Response to Reviewer #1:

First of all, we would like to thank you again for your constructive comments and suggestions. We have tried to address the comments point-by-point below. The reviewer's original comments are in italics. Our responses to reviewer's specific comments are put in a normal font. The added or modified parts in the revised manuscript are highlighted in a red color.

Comment) My comment to include MODIS 3km on the 1st review did not intend to have the authors remove the 10km data, which is still valuable. I would recommend the authors to put back the 10km data keeping the 3km one in Fig 3, I think you can fit 3 scatter plots one next to the other by making them a bit smaller.

Reply) We added MODIS 10 km data in Fig. 3 and modified corresponding sentences. Please check out p. 9, lines 201-202; pp. 9-10, lines 205-207; p. 10, 212-216, and Fig. 3.

Comment) 67-68. 2015 is almost over, please rephrase

Reply) We rephrased the sentence. Please see p. 3, lines 66-67.

Comment) 120-121. The initial aerosol composition was prepared using AOD data from both…

Reply) We rephrased the sentence.

Comment) 154 Meteorological

Reply) We corrected.

Comment) 269. "they require four data assimilation steps" Also, can you provide a reference to such data assimilation system?

Reply) We changed the sentence and added a related reference. Please see p. 12, lines 271-272.

Comment) 294. "for most missing (white) pixels"

Reply) We modified.

Comment) Figure 4. There are no labels to indicate which line represents which observation operator. Also, please include three more panels (you can decrease the size of each panel for a 2x2 view) for the other aerosol species: OC, BC and Sea-salt as is also important to understand the differences between operators and the RH dependence (even if there is none) when these species dominate.

Reply) We modified and added Fig. 4 and corresponding sentence. Please check out p. 15, lines 331 and Fig. 4.

Comment) 358. "of the secondary OA formation"

Reply) We modified.

Comment) 362-363. What is assumed to be equal, the increments or the total concentrations? Is this independent of the background concentrations?

Reply) The mass concentration of surface OAs was changed to be equal to the mass concentration of surface SO_4^{2-}. Therefore, ΔAOD_k (background AOD – ST-kriging AOD) is same as the modified AODs calculated by changed mass concentrations of OAs and SO_4^{2-}. Both mass concentrations are changed independently from the background concentrations. Please check out p. 16, lines 364-368.

Comment) 386. Erase extra space in "3. 5"

Reply) We corrected.

Comment) 587. "smaller"

Reply) We corrected.

GIST-PM-Asia v1: development of a numerical system to improve particulate matter forecasts in South Korea using geostationary satellite-retrieved aerosol optical data over Northeast Asia

S. Lee[1], C. H. Song[1], R. S. Park[1, 5], M. E. Park[1, 6], K. M. Han[1], J. Kim[2], M. Choi[2], Y. S. Ghim[3] and J.-H, Woo[4]

[1]{School of Environmental Science and Engineering, Gwangju Institute of Science and Technology (GIST), Gwangju, 500-712, Korea}

[2]{Department of Atmospheric Sciences, Yonsei University, Seoul, 120-749, Korea}

[3]{Department of Environmental Science, Hankuk University of Foreign Studies, Yongin, 449-791, Korea}

[4]{Department of Advanced Technology Fusion, Konkuk University, Seoul, 143-701, Korea}

[5]{Numerical Model Team, Korea Institute of Atmospheric Prediction Systems (KIAPS), Seoul, 156-849, Korea}

[6]{Asian Dust Research Division, National Institute of Meteorological Research (NIMR), Jeju-do, 697-845, Korea}

Correspondence to: C. H. Song (chsong@gist.ac.kr)

(For submission to **Geoscientific Model Development**)

Abstract

To improve short-term particulate matter (PM) forecasts in South Korea, the initial distribution of PM composition, particularly over the upwind regions, is primarily important. To prepare the initial PM composition, the aerosol optical depth (AOD) data retrieved from a geostationary equatorial orbit (GEO) satellite sensor, GOCI (Geostationary Ocean Color Imager) which covers Northeast Asia (113°E–146°E; 25°N–47°N), were used. Although GOCI can provide a higher number of AOD data in a semi-continuous manner than low Earth orbit (LEO) satellite sensors, it still has a serious limitation in that the AOD data are not available at cloud pixels and over high-reflectance areas, such as desert and snow-covered regions. To overcome this limitation, a spatio-temporal (ST) kriging method was used to better prepare the initial AOD distributions that were converted into the PM composition over Northeast Asia. One of the largest advantages in using the ST-kriging method in this study is that more observed AOD data can be used to prepare the best initial AOD fields compared with other methods that use single frame of observation data around the time of initialization. It is demonstrated in this study that the short-term PM forecast system developed with the application of the ST-kriging method can greatly improve PM_{10} predictions in Seoul Metropolitan Area (SMA), when evaluated with ground-based observations. For example, errors and biases of PM_{10} predictions decreased by ~60% and ~70%, respectively, during the first 6 h of short-term PM forecasting, compared with those without the initial PM composition. In addition, the influences of several factors on the performances of the short-term PM forecast were explored in this study. The influences of the choices of the control variables on the PM chemical composition were also investigated with the composition data measured via PILS-IC and low air-volume sample instruments at a site near Seoul. To

improve the overall performances of the short-term PM forecast system, several future research directions were also discussed and suggested.

Keywords: aerosol optical depth (AOD), short-term PM forecast, CMAQ model simulations, geostationary satellite, spatio-temporal kriging.

1 Introduction

It has been reported that there is a strong relationship between exposure to atmospheric particulate matter (PM) and human health (Brook et al., 2010; Brunekreef and Holgate, 2002; Pope and Dockery, 2006). PM has become a primary concern around the world, particularly in East Asia, where high PM pollution episodes have occurred frequently, mainly due to the large amounts of pollutant emissions from energetic economic activities. In an effort to understand the behaviors and characteristics of PM in East Asia, chemistry-transport models (CTMs) have played an important role in overcoming the spatial and temporal limitations of observations, and also enable policy makers to establish scientific implementation plans via making atmospheric regulations and policies. To improve the performance of the PM simulations, integrated air quality modeling systems that consist of CTMs, meteorological models, emissions, and data assimilation using ground- and satellite-borne measurements have been introduced (Al-Saadi et al., 2005; Park et al., 2011; Song et al., 2008). However, accurate simulations of PM distributions with CTMs have been challenging, because of many uncertainties from emission fluxes, meteorological fields, and chemical and physical parameterizations in the CTMs. For example, the Korean Ministry of Environment (MoE) has recently started to implement air quality forecasts for PM_{10}, $PM_{2.5}$ and ozone over the Seoul metropolitan area (SMA), the largest metropolitan area in South Korea. However, the forecasting accuracy for high PM_{10} alert (81 to 120 μg m^{-3}) in the current system has been low (< 60%) since 2013. Thus, urgent improvements in the PM_{10} predictions are necessary.

In this context, an improved short-term PM forecast system was developed and introduced, based on an analogy to the system of numerical weather prediction (NWP). Figure 1(a) presents a flow diagram of an NWP in which regional meteorological modeling is conducted using two important inputs: (i) boundary conditions (BCs) from global meteorological models and (ii) initial conditions (ICs) prepared via data assimilation using ground-measured data and balloon-, ship-, aircraft-, and/or satellite-borne measurements. In contrast, conventional chemical weather forecast (CWF) (e.g., forecasts for ozone and PM) has been carried out only using meteorological fields and pollutant emissions (Fig. 1(b)). In the short-term PM forecast system proposed here (Fig. 1(c)), one more input is added to the conventional CWF system: the initial distribution of PM composition. To prepare the initial PM composition, a scheme that uses geostationary satellite-derived aerosol optical depths (AODs), is developed in this study. Similarly, the BCs for the CTM runs are obtained from global CTM simulations.

In the improved CWF system, AOD data retrieved from low Earth orbit (LEO) satellite sensors, such as Moderate Resolution Imaging Spectroradiometer (MODIS) and Multi-angle Imaging SpectroRadiometer (MISR) can be used to set up the ICs for the short-term PM forecast (Benedetti et al., 2009; Liu et al., 2011; Saide et al., 2013). While these AOD data have an advantage in spatial coverage compared with those obtained from point stations, the use of the LEO satellite-derived AODs has another limitation in acquiring continuous observations over a certain area due to the capabilities of the LEO sensors in their orbital periods and viewing swath widths.

Such limitations in using LEO satellite observations can be overcome with the help of geostationary (GEO) satellite sensors providing semi-continuous observations over a specific part of the Earth during the day (Fishman et al., 2012; Lahoz et al., 2011; Zoogman et al., 2014). Recently, aerosol optical properties (AOPs) from the Geostationary Ocean Color Imager (GOCI) have become available. GOCI is the first multi-spectral ocean color sensor onboard the Communication, Ocean, and Meteorological Satellite (COMS), launched over Northeast Asia in 2010, providing semi-continuous AOD, single scattering albedo (SSA), and fine mode fraction (FMF) over a domain of Northeast Asia (Lee et al., 2010). With GOCI AOD data, a novel approach was developed to investigate transboundary PM pollution over Northeast Asia (Park et al., 2014a).

In this study, we carried out hindcast studies (forecast studies with past data) to find the "best" method to improve the performance of the short-term PM forecasting using the GOCI AODs. To do this, we developed a model, Geostatistical Interpolation of Spatio-Temporal data for PM forecasting over Northeast Asia (GIST-PM-Asia) v1 that includes: (i) a spatio-temporal kriging (ST-kriging) method to spatio-temporally combine the GOCI-derived AODs, (ii) "observation operators" to convert the CTM-simulated PM composition into AODs and vice versa, and (iii) selection of "control variables" (CVs) through which the distribution of AODs can be converted back into the distributions of the PM composition to be used as the ICs. The uses of the ST-kriging method, observation operators, and CVs are illustrated in Fig. 1. The main advantages of using the ST-kriging method are discussed in detail in the main text. Several sensitivity studies were also conducted to improve the understanding of forecasting errors and biases in the short-term PM forecasting system developed.

With these research objectives and methodology, this paper is organized as follows: the hindcast framework is first described in detail in Sect. 2. In Sect. 3, the hindcast results with various configurations are evaluated with ground-based observations during the high PM episodes in SMA to find the "best" configuration for future short-term PM forecast. After that, a summary and conclusions are provided in Sect. 4.

2 Methodology

The initial aerosol composition was prepared using AOD data from both the GOCI sensor and CTM model simulations. For the CTM simulations, the Community Multi-scale Air Quality (CMAQ; ver. 5.0.1) model (Byun and Ching, 1999; Byun and Schere, 2006) together with the Weather Research and Forecast (WRF; ver. 3.5.1) (Skamarock and Klemp, 2008) were used. The ST-kriging method and 12 different combinations of observation operators and CVs were also used for preparing the distributions of the 3-D PM composition over the GOCI-covered domain. The CMAQ model simulations with the 12 different configurations were carried out and the performances were then tested against ground-measured AOD, PM_{10}, and $PM_{2.5}$ composition. The details of these components are described in the following sections.

2.1 Meteorological and chemistry-transport modeling

The WRF model provided meteorological data with 15 km × 15 km horizontal grid spacing and 26 vertical layers extending up to 50 hPa. To obtain highly-resolved terrestrial input data, the topography height from NASA Shuttle Radar Topography Mission (SRTM) 3 arc-second database (http://dds.cr.usgs.gov/srtm/version2_1/SRTM3) and the land use information provided by Environmental Geographic Information Service (EGIS; http://egis.me.go.kr) were used. Initial and boundary meteorological conditions for the WRF simulation were provided by the National Centers for Environmental Protection (NCEP) final operational global tropospheric analyses (http://rda.ucar.edu/datasets/ds083.2). To improve 3-D temperature, winds and water vapor mixing, objective analysis was employed by incorporating the NCEP ADP Global surface and upper air observation data. The meteorological fields were provided with 1-h temporal resolution, and were then converted into the input fields for the CMAQ model simulations by the Meteorology-Chemistry Interface Processor (MCIP; ver. 4.1) (Otte and Pleim, 2010).

The CMAQ model is a chemistry-transport model that simulates the chemical fates and transport of gaseous and particulate pollutants. In this study, the CMAQ modeling covered Northeast Asia, from 92° to 149° E and 17° to 48° N, using 15 km × 15 km horizontal grid spacing (Fig. 2) with 14 terrain following σ-coordinates, from 1000 to 94 hPa. The configurations of the WRF model and CMAQ simulation used in this study are described in Table 1.

Anthropogenic emission inputs were processed by Sparse Matrix Operator Kernel Emissions in Asia (SMOKE-Asia; ver. 1.2.1), which has been developed for processing anthropogenic emissions for Asia. Details of SMOKE-Asia were described in Woo et al. (2012). Biogenic emissions were prepared using the Model of Emission of Gases and Aerosol from Nature (MEGAN; ver. 2.0.4) (Guenther et al., 2006) with the MODIS-derived leaf area index (Myneni et al., 2002), MODIS land-cover data sets (Friedl et al., 2002), and the meteorological input data described above. For the consideration of biomass burning emissions, daily fire estimates provided by Fire Inventory from NCAR (FINN) were used (Wiedinmyer et al., 2011). Asian mineral dust emissions were not considered in this study. Thus, the periods for model evaluation were selected during periods when mineral dust events did not take place.

To take full advantage of the AOD data sets intensively measured during the Distributed Regional Aerosol Gridded Observation Network in Asia (DRAGON-Asia) campaign, modeling episodes were chosen for the campaign period from 1 March to 31 May 2012. First, background CMAQ model simulations were conducted for the 3-month DRAGON period with 10-day spin-up modeling. After this, initial conditions were prepared using the ST-kriging method, observation operators and CVs via the combination of GOCI AODs with the background modeling AOD. Analysis was carried out for 12-h from 12:00 in local time (LT) on 10 selected high PM pollution days. Each hindcast hour is referred to be H+0 to H+12. In this study we paid more attention to the performance of the first 12-h PM_{10} hindcast results, and the analysis of the hindcast results after 13 h is also discussed briefly in Sect. 3.3.

In the hindcast analysis, different hindcast runs with 12 combinations of different observation operators and CVs were conducted, as discussed in Sect. 2.4 and 2.5. We selected 1 episode from March (28 March), 5 episodes from April (8, 9, 14, 17, and 23 April), and 4 episodes from May (6, 13, 15, and 16 May), 2012 for the analysis associated with three criteria of: (i) on the selected days the average PM_{10} from 12:00 to 18:00 LT was above 70 $\mu g\ m^{-3}$ over SMA, (ii) on the selected days, the daily coverage of the GOCI AOD data was at least 20 % over the GOCI domain, and (iii) on the selected days, dust events were not recorded over South Korea according to the Korea Meteorological Administration (KMA). Additional hindcast runs were also conducted from 7 March 12:00 to 19 March 11:00 for evaluating the performances of the hindcast runs for less polluted episodes. In this study, we focused on SMA, because we were particularly interested in this area. However, the system introduced here can be applied to other areas inside the GOCI domain where surface PM observation data are available.

2.2 Observation data

2.2.1 GOCI AOD

As mentioned previously, GEO satellite sensors have important advantages compared with LEO satellite sensors, such as semi-continuously (with 1-h intervals) producing AOP data over a specific domain of interest. Despite this temporal advantage, it has been difficult for most GEO satellite sensors to produce accurate AOPs, because they have only one or two visible channels. In contrast, the GOCI instrument has six visible and two near-infrared channels, and can produce multi-spectral images eight times per day with a spatial resolution of approximately 500 m × 500 m with coverage of 2,500 km × 2,500 km, including part of Northeast China, the Korean peninsula, and Japan (Fig. 2). Using the 1-h resolved multi-spectral radiance data from GOCI, the uncertainties of AOP retrievals can be dramatically reduced (Park et al., 2014a). The GOCI AOPs were retrieved with multi-channel algorithms that can provide hourly AOP data including AOD, FMF, and SSA at 550 nm (Choi et al., 2015). Compared with the algorithms from two previous studies (Lee et al., 2010, 2012), the GloA2 algorithm uses an improved lookup table for retrieving the AOPs, using extensive observations from Aerosol Robotic Network (AERONET) and monthly surface reflectance observed from GOCI, and provides 1-h resolved AOP data at eight fixed times per day (from 09:30 to 16:30 LT) with 6 km × 6 km spatial resolution. In this study, the AOD data from the GOCI AOPs were used (because the SSA and FMF data need further improvements) and also compared with collection-5.1 10 km MODIS aerosol products from the Aqua and Terra satellites (Levy et al., 2007; Remer et al., 2005) and collection-6 3 km MODIS aerosol products from the Aqua and Terra satellites (Munchak et al., 2013) to present the relative performances of GOCI AOD. The AERONET AOD data were also used for assessing the relative accuracy of the GOCI AODs. Figures 3(a), 3(b), and 3(c) show the scatter plot analyses of three satellite-retrieved 10 km MODIS AODs, 3 km MODIS AODs, and GOCI AODs vs. AERONET level 2 AODs over the GOCI domain during the DRAGON-Asia campaign. All the satellite data were sampled within spatial and temporal differences of 3 km and 10 min from the AERONET observations. It should also be noted that the GOCI and MODIS data were compared with the AERONET data without the applications of kriging method. First, it was found that GOCI provided more frequent AOD data (N = 2276) than 3km MODIS (N = 629) and that GOCI AODs data show comparable regression coefficient (R = 0.85), root mean square error (RMSE = 0.25), and mean bias (MB = -0.19), compared with 3km MODIS data (R = 0.89; RMSE= 0.16; MB = 0.06). This indicates that the GOCI AOD data not only have comparable quality to the MODIS AOD data, but also provide a higher number of data over the GOCI domain. In Fig. 3(d), the daily spatial AOD percent coverages of the Aqua/Terra MODIS and GOCI sensors are compared. It was found that there are a large number of daily missing pixels in the observations of both satellite sensors (the average percent coverages of Aqua MODIS, Terra MODIS and GOCI AODs during the period were about 9%, 10%, and 29%, respectively).

2.2.2 Ground-based observations

AERONET is a global ground-based sunphotometer network managed by the NASA Goddard Space Flight Center, providing spectral AOPs including AOD, SSA, and particle size distributions, available at http://aeronet.gsfc.nasa.gov (Holben et al., 1998). To match the wavelength of GOCI AOD with AERONET AOD, the AOD data at 550 nm were calculated via interpolation, using AODs and Ångström exponent data between 440 and 870 nm from the DRAGON-Asia level 2.0 data. AOD data from 29 AERONET sites inside the GOCI domain were used for validating GOCI and ST-kriging AOD products, and those from six AERONET sites in SMA were selected for evaluating the performance of hindcast AODs.

To analyze hindcast surface aerosol concentrations, the PM_{10} observations provided by the National Ambient Air Monitoring System (NAMIS) network in South Korea were used. The NAMIS network, operated by the MoE has collected air pollutant concentrations of PM_{10} measured by an automatic β-ray absorption method with a detection limit of 2 μg m^{-3} at 5-min intervals. We selected 58 NAMIS sites in SMA, the locations of which are shown in Fig. 2, and used 1-h averaged data for the analysis during the selected episodes.

Ion concentrations of $PM_{2.5}$ were also measured using a particle-into-liquid sampler coupled with ion chromatography (PILS-IC) and a low air-volume sampler with a Teflon filter in Yongin City, located downwind of Seoul (Fig. 2). Details on the measurement methods are described in Lee et al. (2015) and are not repeated here. One-hour averaged sulfate (SO_4^{2-}), nitrate (NO_3^-), and ammonium (NH_4^+) concentrations, measured by the PILS-IC, and 24-h averaged SO_4^{2-}, NO_3^-, NH_4^+, organic carbon (OC), and elementary carbon (EC), measured by the low air-volume sampler, were used for further comparison during the selected episodes (Sect. 3.4). The observed OC concentrations were multiplied by a factor of 1.5, to estimate organic aerosols (OAs) concentrations (He et al., 2011; Huang et al., 2010).

2.3 Spatio-temporal kriging

Kriging is a geostatistical interpolation method to estimate unmeasured variables and their uncertainties, using correlation structure of measured variables. An atmospheric application study of the kriging method to estimating PM_{10} exceedance days over Europe reported that

ST-kriging showed comparable performances to those of the EnKF approach (Denby et al., 2008).

In this study, the ST-kriging method was used to fill out the missing pixels (Fig. 3(d)) with the spatial and temporal GOCI AOD data. The AOD fields produced by ST-kriging can be prepared with a horizontal resolution of 15 km × 15 km from 10:00 LT to 16:00 LT over the GOCI domain. In this study, the AOD data at 12:00 LT (H+0) during the selected episode days were used for preparing the initial conditions. The details and general application of the ST-kriging method are presented in Appendix A. One advantage of using ST-kriging in this study framework is to use large numbers of observational data (GOCI AODs), compared with other methods. In fact, the GOCI AOD data are densely available temporally (with 1-h intervals) and spatially (compared with MODIS AODs; see Figs. 3(a) and 3(b)). This was the primary reason for using the ST-kriging method in this study. For example, when initial AOD fields were prepared at a certain time (e.g., at noon, 12:00 LT: H+0), the ST-kriging method uses not only GOCI AOD data at 11:30 LT or 12:30 LT, but also GOCI AOD data at 09:30, 10:30, and 13:30, unlike other methods. In the case of 4 April, 2012 (a high PM pollution episode during the DRAGON-Asia campaign), other interpolation methods (e.g., Cressman, bilinear, and nearest-neighbor methods) could use only the GOCI AOD data of ~88,000 for the preparation of the initial AOD field at 12:00 LT, whereas the ST-kriging method used the GOCI AOD data of ~280,000 (3 times more AOD data). Sequential data assimilation (DA) methods such as OI and 3DVAR can use the same number of observations as the ST-kriging method. However, they required four data assimilation step (i.e. 4-hour time window for DA) (Tang et al., 2015) to include observations from 09:30 to 13:30, thus greatly increasing the computational cost for daily assimilation.

If the observation data are densely available and the differences between the observations and model-simulated data are large (i.e., the model simulations include relatively large errors and biases), there is less “practical need” to use the CTM-simulated data in the process of data assimilation. That is, it would be more desirable if the values of the unobserved (missing) pixels could be filled in based on “more reliable” observation data (here, GOCI AODs). This would be particularly true, when the CTM-predicted AODs are systematically underestimated compared with GOCI or AERONET AODs (as will be shown in Fig. 5(a)). Additionally, computation costs of the ST-kriging method are so low that the ST-kriging AOD can be calculated rapidly. For example, the 1-day process for preparing the AOD fields over the GOCI domain takes only ~20 min with two 3.47 GHz Xeon X5690 6-core processors and 32 gigabytes memory in the current application of the ST-kriging method. Thus, it can be applied directly to the daily CWF due to the relatively cheap computation cost. Again, computation time (rapid calculation) is a central issue in daily (short-term) chemical weather forecasts. The calculation of daily three-dimensional semivariogram takes most of the computation time (regarding the details of calculation of the daily three-dimensional semivariogram, refer to Appendix A and Fig. A1).

Connected with these discussions, in the application of the ST-kriging method to the GOCI AODs, the “optimal number” of observation data is necessary to balance the accuracy of the data and the computational speed. From many sensitivity tests (not shown here), the optimal number of observations for most missing (white) pixels is approximately 100. That is, the use of more observation data above this optimum number does not meaningfully enhance the accuracy of AODs of the missing pixels, but simply takes more computation time. This number of observation data is usually available for the most of the missing (white) pixels of the GOCI scenes from nearby grids both/either at the concurrent scene spatially within ~100 km and/or at the temporally-close snapshots within 3-h. Based on these reasons, the ST-kriging method was chosen for this study.

2.4 Observation operator

An observation operator (or forward operator) describes the relation between observation data and model parameters. For example, the observation operator in this study converts the aerosol composition into AODs (and vice versa). Based on the aerosol composition and the relative humidity (RH) from the model simulations, simulated AODs at a wavelength of 550 nm (τ_{CMAQ}) were calculated with the following observation operator:

$$\tau_{CMAQ} = \sum_{s=1}^{N}\sum_{l=1}^{M} \alpha_{s,dry} f_s(RH_l)[C]_{s,l} H_l \qquad (1)$$

where N and M denote the number of aerosol species (s) and model layer (l), respectively, $\alpha_{s,dry}$ the mass extinction efficiency (MEE) of the species, (s) at 550 nm under the dry condition, $f_s(\mathrm{RH}_l)$ the hygroscopic enhancement factor for the species, (s) as a function of RH at the layer of l, $[C]_{s,l}$ the mass concentration of the species, (s) at the layer of l, and H_l the height of layer l. Here, $[C]_{s,l}$ is selected as the control variable (refer to Sect. 2.5).

In this study, three observation operators were used for calculating AODs and updating initial PM composition for the hindcast studies. The differences in the observation operators are caused mainly by the differences in $\alpha_{s,dry}$ and $f_s(\mathrm{RH}_l)$ of Eq. (1). The first observation operator was selected from Goddard Chemistry Aerosol Radiation and Transport (GOCART) model (Chin et al., 2002; hereafter GOCART operator). Hygroscopic growth rates for SO_4^{2-}, OC, BC, and sea-salt aerosols were considered separately in this operator. The second observation operator was from the GEOS-Chem model (the GEOS-Chem operator). The detailed aerosol speciation and MEE values were described in Martin et al. (2003). Final observation operator is based on the study of Malm and Hand (2007) (the IMPROVE operator). This observation operator was based on the reconstruction method with the MEEs and hygroscopic enhancement factors at 550 nm for different types of aerosol species. Table 2 summarizes the characteristics of the three observation operators chosen in this study. To consistently consider the characteristics of the three observation operators, aerosol types (s in Eq. (1)) were classified into seven groups: SO_4^{2-}, NO_3^-, NH_4^+, OAs, BC, sea-salt, and others, which mainly consist of $PM_{2.5}$ trace elements (Reff et al., 2009). In the classification, internal mixing states of SO_4^{2-}, NO_3^-, and NH_4^+ were assumed. It should also be noted that the consideration of NO_3^- is important to correctly estimate AOD and aerosol mass loading in East Asia (Park et al., 2011, 2014b; Song et al., 2008). Figure 4 shows the wet MEE values ($\alpha_{s,wet}$; product of $\alpha_{s,dry}$ and $f_s(\mathrm{RH}_l)$ in Eq. (1)) calculated for SO_4^{2-}, NO_3^-, and NH_4^+, OAs, BC and sea-salt at a wavelength of 550 nm as a function of RH, indicating that the three different operators can create large differences in the wet MEE values.

2.5 Selection of control variables

To prepare the distributions of the aerosol composition, the ST-kriging AOD fields should be converted into the 3-D aerosol composition. To do this, the differences between the ST-kriging AODs and background AODs (often called "observational increments": $\Delta\mathrm{AOD}_k = \mathrm{AOD}_{\text{ST-kriging},\,k} - \mathrm{AOD}_{\mathrm{bg},k}$, k = grid cell) should be added to the background model-derived aerosol composition at each grid cell, in connection with the observation operators (Eq. (1)). Which aerosol species is/are selected for allocating $\Delta\mathrm{AOD}_k$? We selected four types of control variables (CVs) of particulate species. First, all the particulate species were selected as CVs. In this case, $\Delta\mathrm{AOD}_k$ was distributed to all the particulate species, with the particulate fractions calculated from the background CMAQ model simulations. The second CV was the selection of SO_4^{2-} concentration. Despite the large contribution of SO_4^{2-} to both AOD and PM concentration in East Asia, model-estimated SO_4^{2-} have shown large systematic underestimations, compared with observed SO_4^{2-} concentrations (Park et al., 2011, 2014b). This can be related to either (or both) the uncertainty in SO_2 emissions in East Asia or (and) the uncertainty in the parameterizations of SO_4^{2-} production in the CTM models (Kim et al., 2013; Lu et al., 2010; Smith et al., 2011; Park et al., 2014). In addition, there is also large uncertainty in the levels of hydroxyl radicals (OH) due to uncertain daytime HONO chemistry, OH reactivation, in-plume process and others (Archibald et al., 2010; Han et al., 2015; Karamchandani et al., 2000; Kim et al., 2009; Kubistin et al., 2010; Lelieveld et al., 2008; Song et al., 2003, 2010; Sörgel et al., 2011; Stemmler et al., 2006; Zhou et al., 2011). Obviously, these uncertainties can influence the levels of H_2SO_4 and thus particulate sulfate concentrations in the atmosphere. In this case, aerosol mass concentrations (except for SO_4^{2-}) were the same as those of the background aerosol concentrations. Third, SO_4^{2-} and OAs were chosen to be changed. Although OAs are one of the major particulate species, it is well-known that OAs concentrations are also systematically underestimated due to two reasons: (i) the uncertainty in the parameterizations of the secondary OA formation (Donahue et al., 2006, 2011; Dzepina et al., 2009; Hodzic et al., 2010; Matsui et al., 2014; Slowik et al., 2010), and (ii) the uncertainty in emission inventories for anthropogenic and biogenic OA precursors (Guenther et al., 1999; Han et al., 2013; Sakulyanontvittaya et al., 2008; Tsimpidi et al., 2010; Wyat Appel et al., 2008). In this case, the mass concentration of surface OAs is assumed to be equal to the mass concentration of surface SO_4^{2-}, based on the ground-based measurement studies over East Asia (Lee et al., 2009; Zhang et al., 2007, 2012). Thus, ΔAOD_k is accounted for the increments of concentrations from OAs and SO_4^{2-} which are changed independently from the background concentrations. Finally, SO_4^{2-}, NO_3^-, NH_4^+, and OAs were selected to be changed. In this case, ΔAOD_k was distributed to the selected four species, with the fractions of SO_4^{2-}, NO_3^-, NH_4^+ calculated from background simulations. The method to change the OA concentration in the fourth selection of CVs was the same as the method in the third selection of CVs. The fourth selection of CVs was also made to consider thermodynamic balance among SO_4^{2-}, NO_3^-, and NH_4^+ concentrations (Bassett and Seinfeld, 1983; Saxena et al., 1986; Seinfeld and Pandis, 2012; Song and Carmichael, 1999; Stelson et al., 1984). It should be noted that background modeling-derived vertical profiles and the size distributions of aerosol species were used for converting 2-D AOD to 3-D PM composition in all the STK cases. With the combinations of the three different observation operators and four choices of CVs (Table 3), 12 hindcast runs were made for high PM episodes during the DRAGON-Asia campaign.

3 Results and Discussion

In Sect. 3, the performances of ST-kriging method are evaluated via comparisons with the AERONET AOD in the GOCI domain (Sect. 3.1). Sensitivity analyses were then conducted to examine the impacts of the observation operators and CVs on the accuracy of the hindcast runs (Sect. 3.2). After that, the overall performances of the hindcasts were evaluated with ground-based observations during the high PM_{10} episodes over SMA (Sect. 3.3). A comparative analysis of the PM composition between hindcast results and observations was also conducted to further investigate/analyze the performance of the hindcast system (Sect. 3.4). In addition, hindcast results for the periods of less polluted episodes are also shown with the best configuration (Sect. 3.5).

3.1 Evaluation of ST-kriging AODs

Figure 5(a)-(c) show scatter plot analyses of background CMAQ-simulated AODs, spatial kriging AODs (i.e., kriging only with the GOCI AODs from one scene) and ST-kriging AODs vs. AERONET level 2 AODs over the GOCI domain during the DRAGON-Asia campaign. First, it can be found that the CMAQ-predicted AODs are underestimated significantly compared with the AERONET AODs. As discussed in Sect. 2.3, this was the main reason that we used the ST-kriging method in this study. More weight should be given to observations, because the CTM modelling produces significant biases. Second, ST-kriging AODs show improved correlations, compared with the AODs estimated via the spatial kriging method. Also, the ST-kriging AOD data show equivalent levels of errors and biases, compared with GOCI AOD data. If one compares Fig. 3(b) with Fig. 5(c), it can be seen that the ST-kriging can effectively produce the AOD fields (also note the increase in N).

Figures 5(d) and (e) show the scatter plot analysis of the ST-kriging AOD products versus the AERONET AOD data with kriging variances (KVs). It is found that the ST-kriging AOD data with KV ≤ 0.04 show similar scattering pattern and accuracy to those of GOCI AOD. In contrast, some overestimated outliers from the ST-kriging AOD data in Fig. 5(e) (e.g., 1.0-2.0 in the x-axis and 2.0-4.0 in the y-axis) show different patterns than those from the GOCI AOD data. This may be explained by the relatively large KVs (> 0.04) of such overestimated outliers. The KV generally increases when the observations near a certain prediction point are not available or when nearby observations have relatively large errors. Thus, when the GOCI observations are contaminated by optically thin clouds and they are not removed perfectly, this can increase the local variances due to their high cloud optical depth (COD). These factors can affect the quality of the ST-kriging AOD products. In this study, only the ST-kriging AOD products having small KVs (less than 0.04) were used for preparing the initial condition of each data processing step. Therefore, the initial PM concentrations did not changed where the ST-kriging AOD having large KVs (larger than 0.04). Collectively, it appears that the ST-kriging method is a reasonable tool for obtaining realistic AOD values at locations where the GOCI observations are not available.

3.2 Sensitivity of observation operators and control variables to AOD and PM_{10} predictions

To investigate the best combination of the observation operators and CVs, the AOD and PM_{10} hindcast runs and sensitivity analyses with the 12 different configurations (Table 3) were performed. For this, the hindcast AOD and PM_{10} from 13:00 LT to 19:00 LT (H+1 to H+6) on 10 selected episode days were compared with the ground-measured AOD and surface PM_{10}. The observations from the six AERONET sites and nearest NAMIS PM_{10} stations within 10 km from the AERONET locations were selected for this comparison study (Fig. 2). The AOD values for the background CMAQ model simulations without the application of the ST-kriging method (noSTK) were also calculated with the GEOS-Chem observation operator.

Figure 6 shows the soccer plot analysis of the 13 hindcast AODs (left panel) and PM_{10} (right panel) during the first 6-h of the short-term PM hindcasting on the 10 selected episode days. In the soccer plot, mean fractional bias (MFB) and mean fractional error (MFE) (described in Appendix B) are plotted on the x- and y-axes, respectively. Using this plot, the relative discrepancy can be presented by the distances from the origin of the plot, and particular characteristic, such as systematic bias, can also be shown as a group of scatter points. Detailed statistical metric values are shown in Table 4. All the AODs and PM_{10} with the application of the ST-kriging method (STK) are much better than those from the noSTK simulation, with reduced errors and biases. Percentage decreases in MFE with the STK hindcasts were found to be 60-67% for AOD and are 50-63% for PM_{10}. The MFB also decreased by 67-82% for AOD and by 56-84% for PM_{10}. The noSTK case showed a strong negative bias (i.e., underprediction) and the 12 STK cases also showed less, yet still negative, biases. These negative biases are considered to be systematic, because of the negative bias of the GOCI AOD data (Fig. 6). Additionally, the negative biases are due to underestimation of CMAQ-simulated SO_4^{2-} and OAs concentrations (Carlton et al., 2008, 2010; Park et al., 2011, 2014b). This issue has been discussed in Sect. 2.5 and is investigated further in Sect. 3.4.

On the other hand, there are relatively small differences in errors and biases among the 12 STK cases (Fig. 6). Several differences among the 12 sensitivity cases were investigated further. First, the error and bias patterns for the AOD values were different from those for the PM_{10} predictions, being associated with the different observation operators. For example, the STK cases with the IMPROVE observation operator (cases C1, C2, C3, and C4) exhibited a relatively small bias for PM_{10} predictions, although they did not in the AOD predictions. This was likely caused by small wet MEE values of SO_4^{2-}, NO_3^-, and NH_4^+ in the IMPROVE observation operator (represented by the green line in Fig. 4). By Eq. (1), the concentrations of converted aerosol species are inversely proportional to the MEEs of aerosol species. In the CV cases, the selections of SO_4^{2-} and OAs (i.e., A3, B3, and C3) and SO_4^{2-}, NO_3^-, NH_4^+, and OAs (i.e., A4, B4, and C4) showed better performances for both the AOD and PM_{10} predictions.

To show the degree of enhanced performances via using the ST-kriging GOCI data, we also carried out some hindcast simulations, using the initial conditions prepared with single-frame GOCI data at 11:30 LT. The grids that did not have AOD observations were not filled out in this runs. In Fig. 6, the MFBs and MFEs of the bilinear interpolation method (denoted as BL) were -45.05 and 59.52 for AOD and -46.13 and 53.30 for PM_{10}, respectively. It is shown in

Fig. 6 that the use of the single-frame GOCI data without filling any gap cannot sufficiently improve the performance, compared with the cases of the STK simulations.

Figure 7 shows the performances of the short-term hindcast system with the 13 different configurations via comparisons between the hourly-averaged PM_{10} observations and model PM_{10} predictions at the six NAMIS sites, on 9 April, 6 May and 16 May, 2012, respectively. Only 3-day and six-site results were selected and presented here, and more comprehensive performance evaluations are presented in Sect. 3.3. While noSTK failed to reproduce the high PM pollutions, all the STK cases showed significant improvements in the surface PM_{10} predictions. However, there was a tendency that the hourly peaks of PM_{10} were not well captured by the STK cases.

Consequently, it can be concluded that the combination of GOCART observation operator and CVs of SO_4^{2-} and OAs (represented by A3) leads to the best results in the current hindcast system (Table 4). The use of the GOCART observation operator and CVs of SO_4^{2-}, NO_3^-, NH_4^+, and OAs (represented by A4) could also provide comparable performance to A3. However, it appears that the differences among the 12 STK cases were relatively small.

3.3 Overall performance evaluation of PM_{10} hindcast over SMA

In this section, PM_{10} from the hindcast experiments were compared with the PM_{10} observations from "58 NAMIS sites" to evaluate the overall performance of the current hindcast system in SMA. Table 5 provides the statistical metrics that were calculated separately from the first and the second 6-h hindcast results. The main characteristics of the statistical analysis in Table 5 are similar to those at the six sites discussed in the previous section. First, both errors and biases of PM_{10} distributions were significantly reduced after the application of the ST-kriging method. The MFEs and MFBs in the 12-h STK simulations decreased by ~40% and ~80%, respectively.

A distinctive difference was also found in the model performances for the first and the second 6-h runs. During the first 6-h, all the hindcast results showed negative biases, with the MFB of ~ -100% for the noSTK cases and ~ -40% for the STK cases. The performances of the A3 and A4 cases are somewhat better than those of the other STK cases (Table 5). Collectively, the MFEs and MFBs of the STK cases are a factor of 2-4 smaller than those of the noSTK cases during the first 6-h.

Figure 8 shows a comparison between the noSTK case and the A3 case, in terms of the PM_{10} predictions, during the first and the next 6 h in SMA with the 6-h averaged NAMIS PM_{10} observations. As shown, the A3 case produced better PM_{10} predictions during the first and the next 6 h. In addition, the A4 case (not shown) also provided similar results to the A3 case, as discussed in Sect. 3.2. It can be confirmed again that the A3 and A4 cases are able to produce better PM_{10} predictions against the PM_{10} observations in SMA.

Hindcast performances from H+13 to H+24 were also evaluated with the ground-measured NAMIS PM_{10} data. In short, the differences between all the STK and noSTK cases became smaller than those during the first 12 h (approximate difference of 10% was found at H+24, i.e., 24 h after the hindcast actually began). Based on this, it appears that the effects of using the initial PM composition on the hindcast performances may effectively last during the first 12 h. After 12 h, the effects started to diminish. This is due to several facts: (i) the regions for applying the initial PM composition in this study were limited only within the GOCI domain (relatively small region); (ii) although the initial PM composition was used, its effects can be offset by uncertainties and errors in emissions as time progressed; and (iii) the large uncertainties associated with the formation of SO_4^{2-} and OAs in the CTMs can also limit the effects of the initial PM composition. The second and the third are the reasons that there is strong necessity for both emissions and CTMs to be improved continuously, even though the initial PM composition is applied in the short-term forecast activities.

3.4 Evaluation of hindcast performance with observed PM composition

In the previous section, PM_{10} mass concentrations were simply predicted by the short-term hindcast system with 12 different combinations of observation operators and CVs. Although the purpose of this study is to develop a better PM forecast system for accurately predicting "PM_{10} mass" concentrations, it is still necessary to more carefully scrutinize the changes in the "PM composition" in accordance with the different selections of the CVs.

During the DRAGON-Asia campaign, the $PM_{2.5}$ composition was measured for SO_4^{2-}, NO_3^-, and NH_4^+ with 30-min intervals and for SO_4^{2-}, NO_3^-, NH_4^+, OC and BC with 24-h intervals using PILS-IC instrument (semi-continuous measurements) and low air-volume sampler with a Teflon filter (off-line measurements), respectively, in Yongin City near SMA (Fig. 2). Thus, in this section, the selection of the CVs is further discussed with the observed $PM_{2.5}$ composition.

Figure 9 shows the comparison between 1-h averaged SO_4^{2-}, NO_3^-, and NH_4^+ concentrations measured via the PILS-IC instrument and model-predicted concentrations during the selected days at the Yongin observation site. Only the STK cases with the GOCART observation operator (i.e., A1, A2, A3, and A4) were selected here. The STK cases showed significant changes in the PM composition with the selection of CVs. For example, the A2 and A3 cases tended to overestimate the SO_4^{2-} concentrations but underestimated the NO_3^-, and NH_4^+ concentrations, whereas the A1 and A4 cases tended to relatively well capture the trend of the concentrations of the three particulate species. This phenomenon was driven by intra-particulate thermodynamics. That is, if larger amounts of SO_4^{2-} are allocated into particles (like the cases of A2 and A3), then NO_3^- tends to be evaporated, because SO_4^{2-} is more strongly associated with NH_4^+ (Song and Carmichael, 1999). As shown in Fig. 9 (a) and (b), when the SO_4^{2-} concentrations increases (as in case A2), the NO_3^- concentrations decrease accordingly, because NO_3^- is evaporated out of the particulate phase as a form of HNO_3 (Song and Carmichael, 1999, 2001). Collectively, the "best" results were produced from the case A4, as shown in Figs. 9(a) - (c).

The 24-h averaged $PM_{2.5}$ compositions measured from the PILS-IC instrument and the low air-volume sampler with a Teflon filter during the campaign period are also compared in Fig. 9(d). Again, the observations of the SO_4^{2-}, NO_3^-, and NH_4^+ concentrations were obtained from both the PILS-IC instrument and the low volume sampler, whereas the concentrations of OAs ($\cong$ [OC] $\times$ 1.5) and EC were only measured via the low air-volume sampler. As shown in Fig. 9(d), the SO_4^{2-}, NO_3^-, and NH_4^+ concentrations from both samplers showed good agreements (see circles and crosses in Fig. 9(d)). The A4 case (the red bars in Fig. 9(d)) again showed the best results in the comparison between the observed and predicted particulate composition, particularly in SO_4^{2-} and OAs. In the previous discussion (see Sect. 3.2 and 3.3), the A3 and A4 cases showed the best performances for predicting "PM_{10} mass concentrations" over SMA. This is somewhat consistent with our analysis in this section. However, in case of the A3, it can capture the PM mass behaviors (Sect. 3.3) but does not capture the changes in the PM composition well (this section). Based on this, it is concluded that the A4 case would be the best configuration for accurately predicting the PM composition as well as the PM mass. However, this PM composition analysis was conducted with only one site observations (Yongin City) in this study. Thus, to reach a firmer conclusion, more intensive analyses with multiple site observations are required in future.

3.5 Evaluation of short-term hindcast performances

To further evaluate the performance of the short-term hindcast runs, 48-hour hindcast simulations with the configuration of A4 were carried out from 7 March to 19 March. The observations from the 6 AERONET sites and the nearest NAMIS stations were analyzed in this study.

The time-series of the first and the second 24-hour averaged PM_{10} at the six sites on 8, 10, and 11 March, 2012 are presented in Fig. 10. Again, reduced errors and biases were shown in the A4 STK simulations, compare with the noSTK simulation for polluted episodes ((a) and (b) in Fig. 10) and for less polluted episode ((c) in Fig. 10). Percent decreases with MFEs of the first 24-hour A4 STK hindcast were ~40% for AOD and ~10% for PM_{10}, and those with MFBs were ~40% for AOD and ~100% for PM_{10}. In addition, slight improvements in the horizontal distributions of AOD and PM_{10} were also found. This was indicated by the increases of correlation coefficients (refer to Table S1). The second 24-hour STK hindcasts also reduced the errors and biases for AOD and PM_{10}, although the improvements in the spatial distributions were not shown clearly. A more detailed statistical metrics is presented in the supplement (Table S1).

4 Summary and Conclusions

For the purpose of improving the performance of short-term PM forecast in Korea, an integrated air quality modeling system was developed with the application of the ST-kriging method using the geostationary satellite-derived AOD data over Northeast Asia. The errors and biases of the ST-kriging AOD showed relatively good agreement, compared with the AERONET observations. With the combinations of the ST-kriging method along with various observation operators and control variables (CVs), the errors and biases of AOD and PM_{10}

predictions can be reduced significantly. It was shown that the selection of the observation operators greatly influence the performances of the STK hindcast systems. On the other hand, the choice of CVs tends to affect PM composition. The combination of the GOCART observation operator and the selection of CVs of SO_4^{2-} and OAs (case A3) was found to be the best one for the PM_{10} mass prediction. All the hindcast runs with the application of the ST-kriging, however, generally showed negative biases (i.e. under-predictions). This was primarily due to the underestimation of the GOCI AOD.

Reducing errors and biases in the current system is important for further development of the PM forecast system. One of the potential methods for reducing the errors and biases is to introduce the MODIS AOD data into the ST-kriging stage, together with the GOCI data. It is expected that this will be able to further reduce the systematic biases, due to the relatively smaller biases of MODIS AOD (as shown Fig. 3). In addition, the combination of the GOCART observation operator and the selection of CVs of SO_4^{2-}, NO_3^-, NH_4^+, and OAs (Case A4) was found to give the "best" results for the prediction of particulate composition at one observation site. However, more intensive measurements of the PM composition are needed for reaching a more solid conclusion.

The ST-kriging AODs used in the current study are expected to be used in other data assimilation methods. For example, in the 3DVAR method, the observation error covariance matrix, which presents the degree of errors of the observations, has been usually assumed by linear equations or single constant value (Liu et al., 2011; Schwartz et al., 2012; Shi et al., 2011). However, as discussed with KVs in Sect. 3.1, the error covariance of the AOD observations can be improved, and the use of the improved observation error covariance matrix can help to prepare more accurate AOD fields, for example, via a 3DVAR method. This study is now underway.

In future, planned GEO satellite sensors will give other opportunities to use semi-continuous AOD observations at high spatial and temporal resolutions. Upcoming GEO satellite sensors scheduled for launch between 2018 and 2020 include NASA's Tropospheric Emissions: Monitoring of Pollution (TEMPO) over North America, ESA's Sentinel-4 over Europe, and Korea Aerospace Research Institute (KARI)'s Geostationary Environment Monitoring Spectrometer (GEMS) over Asia. In the case of the GEMS instrument, it is being designed to provide backscattered UV/Vis radiances between 300 and 500 nm with a spatial resolution of 5 km × 5 km over a large part of Asia. Using advanced observations from the GEMS sensor, it is anticipated that the system developed here will be able to make significant contributions to further improvements in the performances of the PM forecasting system in Asia. This improved PM predictions and modeling framework can also be a core part for entire air quality forecasting system, a more comprehensive health impact assessments, and radiative forcing estimation over (East) Asia in future.

Appendix A: Spatio-temporal kriging method

The ST-kriging methods assume that measured variables in space and time ($\tau(s, t)$) can be regarded as a random function, consisting of a trend component (m) and residual component (ϵ) of which the mean is zero:

$$\tau(s,t) = m(s,t) + \varepsilon(s,t)\,. \tag{A1}$$

The unobserved value $\tau^*(s, t)$ can be averaged with weight using measured values from the surrounding:

$$\tau^*(s,t) = \sum_{i=1}^{n} \tau(s_i, t_i) w_i(s,t) \tag{A2}$$

where n is the number of observations in local neighborhood and $w_i(s, t)$ is the kriging weight assigned to $\tau(s_i, t_i)$. The kriging weight is determined by a theoretical semivariogram.

In case of spatial kriging ($\tau(s)$), the semivariogram (γ) is the best fit to the semivariance (γ^*) as a function of spatial lag (h). Assuming the trend component $m(s)$ in $\tau(s)$ is constant over the local domain (i.e., the ordinary kriging method), the semivariance is defined as:

$$\gamma^*(h) = \frac{1}{2N(h)} \sum_{i=1}^{N(h)} [\tau(s_i) - \tau(s_i + h)]^2 = \frac{1}{2N(h)} \sum_{i=1}^{N(h)} [\varepsilon(s_i) - \varepsilon(s_i + h)]^2 \tag{A3}$$

where $N(h)$ is the number of paired observations at a spatial distance of h, and $\tau_i(s_i + h)$ is the ith observation (in this study, AOD) separated by h from the observation located at s_i. The semivariogram is then depicted by a theoretical model which is the best-fitting curve to the semivariance by minimizing the least square error. For example, a spherical semivariogram (γ), which is commonly used in the theoretical models of the atmospheric studies, is estimated by finding optimal three parameters: (i) nugget (c_n); (ii) range (a); and (iii) partial sill (σ_0^2):

$$\gamma(h) = c_n + \sigma_0^2 [\frac{3h}{2a} - \frac{h^3}{2a^3}] \ (for\, h \le a),\ \gamma(h) = c_n + \sigma_0^2 \ (for\, h > a)\,. \tag{A4}$$

The range parameter indicates the maximum lag in which the variation of semivariogram is meaningful (Cressie, 1992).

To combine the spatial and temporal data for preparing the spatio-temporal semivariograms, the temporal information can be converted into the spatial information (Gräler et al. (2012). First, the spatial and temporal semivariograms are estimated independently using the spherical model from the daily GOCI AOD data. Second, the ratio of spatial range parameter (a_s) of the spatial semivariogram to temporal range parameter (a_t) of the temporal semivariogram (i.e., spatio-temporal scale factor, km h^{-1}) is used to convert the unit of temporal lag into the unit of spatial distance. Consequentially, the 3D spatio-temporal AOD data are converted into the 2-D spatial AOD fields. After that, the spatio-temporal semivariogram is provided to predict the AOD fields with 15 km × 15 km spatial resolution from 10:00 LT to 16:00 LT over the GOCI domain. For the ST-kriging method, the "gstat" (Pebesma, 2004) and the "spacetime" (Pebesma, 2012) software packages in the "R" environment for statistical computing were used (R Development Core Team, 2011). Figure A1 presents an example of the 3D semivariograms from the fitted model (left) and sample from the GOCI data on 8 April. The mean nugget (c_n), range (a), partial sill (σ_0^2) of the spatio-temporal model semivariogram were 0.025, 583km, and 0.227, respectively, during the entire DRAGON-Asia campaign. The average spatio-temporal scale factor of ~34 km h^{-1} was calculated indicating that the AODs observed before or after 1 h at certain location show a similar correlation pattern to those measured simultaneously at ~34 km apart in the ST-kriging model. Figure A2 shows an example of spatial distributions of GOCI AOD from 10:30 to 13:30 LT and ST-kriging AOD at 12:00 LT with a criteria of kriging variances (KVs) less than 0.04.

Appendix B: Statistical metrics

In this study, eight statistical metrics were used for validating the hindcast results (Chai and Draxler, 2014; Savage et al., 2013; Willmott, 1981; Willmott et al., 2009; Willmott and Matsuura, 2005).

Index of agreement (IOA) = $$1-\frac{\sum_{i=1}^{N}(O_i-M_i)^2}{\sum_{i=1}^{N}\left(\left|O_i-\overline{O_i}\right|+\left|M_i-\overline{M_i}\right|\right)^2} \qquad \text{(B1)}$$

Mean fractional error (MFE) = $\frac{1}{N}\sum_{i=1}^{N}\frac{|M_i - O_i|}{\left(\frac{M_i + O_i}{2}\right)}\times 100$ (B2)

Mean fractional bias (MFB) = $\frac{1}{N}\sum_{i=1}^{N}\frac{(M_i - O_i)}{\left(\frac{M_i + O_i}{2}\right)}\times 100$ (B3)

Regression coefficient (R) = $\frac{\sum_{i=1}^{N}(O_i - \overline{O_i})(M_i - \overline{M_i})}{\sqrt{\sum_{i=1}^{N}(O_i - \overline{O_i})^2}\sqrt{\sum_{i=1}^{N}(M_i - \overline{M_i})^2}}$ (B4)

Root mean square error (RMSE) = $\sqrt{\frac{1}{N}\sum_{i=1}^{N}(M_i - O_i)^2}$ (B5)

Mean normalized error (MNE) = $\frac{1}{N}\sum_{i=1}^{N}\left(\frac{|M_i - O_i|}{O_i}\right)\times 100$ (B6)

Mean bias (MB) = $\frac{1}{N}\sum_{i=1}^{N}(M_i - O_i)$ (B7)

Mean Normalized bias (MNB) = $\frac{1}{N}\sum_{i=1}^{N}\left(\frac{M_i - O_i}{O_i}\right)\times 100$ (B8)

where N is the number of data and M_i and O_i are the model value and observation, respectively. The value highlighted by overbar means the arithmetic mean of the data.

Code Availability

WRF and CMAQ source codes and R and NCL computer languages are available to the public. The source codes and computer languages may be downloaded by following instructions found at:

http://www2.mmm.ucar.edu/wrf/users/downloads.html for WRF, https://www.cmascenter.org/cmaq for CMAQ,

http://cran.r-project.org for R, and

https://www.ncl.ucar.edu/Download for NCL.

ST-kriging module code used in this study was based on the instruction of Pebesma (2012) available at http://www.jstatsoft.org/v51/i07, and can be obtained by contacting S. Lee (noitul5@gist.ac.kr).

Acknowledgements

This research was supported by the GEMS program of the Ministry of Environment, South Korea, as part of the Eco Innovation Program of KEITI (2012000160004). This work was also funded by the Korea Meteorological Administration Research and Development Program under Grant KMIPA 2015-5010 and was partly supported by National Institute of Environmental Research (NIER). We thank all PI investigators and their staff for establishing and maintaining the AERONET sites of DRAGON-NE Asia 2012 campaign used in this study. We also thank the MODIS science team for providing valuable data for this research. NCL (2014) was used to draw the figures. The third author is supported by the R&D project on the development of global numerical weather prediction systems of Korea Institute of Atmospheric Prediction Systems (KIAPS) funded by Korea Meteorological Administration (KMA).

References

Archibald, A. T., Cooke, M. C., Utembe, S. R., Shallcross, D. E., Derwent, R. G. and Jenkin, M. E.: Impacts of mechanistic changes on HOx formation and recycling in the oxidation of isoprene, Atmos. Chem. Phys., 10(17), 8097–8118, doi:10.5194/acp-10-8097-2010, 2010.

Bassett, M. and Seinfeld, J. H.: Atmospheric equilibrium model of sulfate and nitrate aerosols, Atmos. Environ. 1967, 17(11), 2237–2252, doi:10.1016/0004-6981(83)90221-4, 1983.

Benedetti, A., Morcrette, J.-J., Boucher, O., Dethof, A., Engelen, R. J., Fisher, M., Flentje, H., Huneeus, N., Jones, L., Kaiser, J. W., Kinne, S., Mangold, A., Razinger, M., Simmons, A. J. and Suttie, M.: Aerosol analysis and forecast in the European Centre for Medium-Range Weather Forecasts Integrated Forecast System: 2. Data assimilation, J. Geophys. Res. Atmospheres, 114(D13), D13205, doi:10.1029/2008JD011115, 2009.

Brook, R. D., Rajagopalan, S., Pope, C. A., Brook, J. R., Bhatnagar, A., Diez-Roux, A. V., Holguin, F., Hong, Y., Luepker, R. V., Mittleman, M. A., Peters, A., Siscovick, D., Smith, S. C., Whitsel, L. and Kaufman, J. D.: Particulate Matter Air Pollution and Cardiovascular Disease An Update to the Scientific Statement From the American Heart Association, Circulation, 121(21), 2331–2378, doi:10.1161/CIR.0b013e3181dbece1, 2010.

Brunekreef, B. and Holgate, S. T.: Air pollution and health, The Lancet, 360(9341), 1233–1242, doi:10.1016/S0140-6736(02)11274-8, 2002.

Byun, D. and Schere, K. L.: Review of the governing equations, computational algorithms, and other components of the models-3 Community Multiscale Air Quality (CMAQ) modeling system, Appl. Mech. Rev., 59(1-6), 51–76, doi:10.1115/1.2128636, 2006.

Byun, D. W. and Ching, J. K. S.: Science algorithms of the EPA Models-3 community multiscale air quality (CMAQ) modeling system, 1999.

Carlton, A. G., Turpin, B. J., Altieri, K. E., Seitzinger, S. P., Mathur, R., Roselle, S. J. and Weber, R. J.: CMAQ Model Performance Enhanced When In-Cloud Secondary Organic Aerosol is Included: Comparisons of Organic Carbon Predictions with Measurements, Environ. Sci. Technol., 42(23), 8798–8802, doi:10.1021/es801192n, 2008.

Carlton, A. G., Bhave, P. V., Napelenok, S. L., Edney, E. O., Sarwar, G., Pinder, R. W., Pouliot, G. A. and Houyoux, M.: Model Representation of Secondary Organic Aerosol in CMAQv4.7, Environ. Sci. Technol., 44(22), 8553–8560, doi:10.1021/es100636q, 2010.

Chai, T. and Draxler, R. R.: Root mean square error (RMSE) or mean absolute error (MAE)? – Arguments against avoiding RMSE in the literature, Geosci. Model Dev., 7(3), 1247–1250, doi:10.5194/gmd-7-1247-2014, 2014.

Chin, M., Ginoux, P., Kinne, S., Torres, O., Holben, B. N., Duncan, B. N., Martin, R. V., Logan, J. A., Higurashi, A. and Nakajima, T.: Tropospheric Aerosol Optical Thickness from the GOCART Model and Comparisons with Satellite and Sun Photometer Measurements, J. Atmospheric Sci., 59(3), 461–483, doi:10.1175/1520-0469(2002)059<0461:TAOTFT>2.0.CO;2, 2002.

Choi, M., Kim, J., Lee, J., Kim, M., Je Park, Y., Jeong, U., Kim, W., Holben, B., Eck, T. F., Lim, J. H., and Song, C. K.: GOCI Yonsei Aerosol Retrieval (YAER) algorithm and validation during DRAGON-NE Asia 2012 campaign, Atmos. Meas. Tech. Discuss., 8, 9565-9609, doi:10.5194/amtd-8-9565-2015, 2015.

Cressie, N.: Statistics for Spatial Data, Terra Nova, 4(5), 613–617, doi:10.1111/j.1365-3121.1992.tb00605.x, 1992.

Denby, B., Schaap, M., Segers, A., Builtjes, P. and Horálek, J.: Comparison of two data assimilation methods for assessing PM_{10} exceedances on the European scale, Atmos. Environ., 42(30), 7122–7134, doi:10.1016/j.atmosenv.2008.05.058, 2008.

Donahue, N. M., Robinson, A. L., Stanier, C. O. and Pandis, S. N.: Coupled Partitioning, Dilution, and Chemical Aging of Semivolatile Organics, Environ. Sci. Technol., 40(8), 2635–2643, doi:10.1021/es052297c, 2006.

Donahue, N. M., Epstein, S. A., Pandis, S. N. and Robinson, A. L.: A two-dimensional volatility basis set: 1. organic-aerosol mixing thermodynamics, Atmos. Chem. Phys., 11(7), 3303–3318, doi:10.5194/acp-11-3303-2011, 2011.

Dzepina, K., Volkamer, R. M., Madronich, S., Tulet, P., Ulbrich, I. M., Zhang, Q., Cappa, C. D., Ziemann, P. J. and Jimenez, J. L.: Evaluation of recently-proposed secondary organic aerosol models for a case study in Mexico City, Atmos. Chem. Phys., 9(15), 5681–5709, doi:10.5194/acp-9-5681-2009, 2009.

Fishman, J., Iraci, L. T., Al-Saadi, J., Chance, K., Chavez, F., Chin, M., Coble, P., Davis, C., DiGiacomo, P. M., Edwards, D., Eldering, A., Goes, J., Herman, J., Hu, C., Jacob, D. J., Jordan, C., Kawa, S. R., Key, R., Liu, X., Lohrenz, S., Mannino, A., Natraj, V., Neil, D., Neu, J., Newchurch, M., Pickering, K., Salisbury, J., Sosik, H., Subramaniam, A., Tzortziou, M., Wang, J. and Wang, M.: The United States' Next Generation of Atmospheric Composition and Coastal Ecosystem Measurements: NASA's Geostationary Coastal and Air Pollution Events (GEO-CAPE) Mission, Bull. Am. Meteorol. Soc., 93(10), 1547–1566, doi:10.1175/BAMS-D-11-00201.1, 2012.

Friedl, M. A., McIver, D. K., Hodges, J. C. F., Zhang, X. Y., Muchoney, D., Strahler, A. H., Woodcock, C. E., Gopal, S., Schneider, A., Cooper, A., Baccini, A., Gao, F. and Schaaf, C.: Global land cover mapping from MODIS: algorithms and early results, Remote Sens. Environ., 83(1–2), 287–302, doi:10.1016/S0034-4257(02)00078-0, 2002.

Gräler, B., Gerharz, L. and Pebesma, E.: Spatio-temporal analysis and interpolation of PM_{10} measurements in Europe, [online] Available from: http://acm.eionet.europa.eu/reports/ETCACM_TP_2011_10_spatio-temp_AQinterpolation, 2012.

Guenther, A., Baugh, B., Brasseur, G., Greenberg, J., Harley, P., Klinger, L., Serça, D. and Vierling, L.: Isoprene emission estimates and uncertainties for the central African EXPRESSO study domain, J. Geophys. Res. Atmospheres, 104(D23), 30625–30639, doi:10.1029/1999JD900391, 1999.

Guenther, A., Karl, T., Harley, P., Wiedinmyer, C., Palmer, P. I. and Geron, C.: Estimates of global terrestrial isoprene emissions using MEGAN (Model of Emissions of Gases and Aerosols from Nature), Atmos. Chem. Phys., 6(11), 3181–3210, doi:10.5194/acp-6-3181-2006, 2006.

Han, K. M., Park, R. S., Kim, H. K., Woo, J. H., Kim, J. and Song, C. H.: Uncertainty in biogenic isoprene emissions and its impacts on tropospheric chemistry in East Asia, Sci. Total Environ., 463-464, 754–771, doi:10.1016/j.scitotenv.2013.06.003, 2013.

Han, K. M., Lee, S., Chang, L. S. and Song, C. H.: A comparison study between CMAQ-simulated and OMI-retrieved NO_2 columns over East Asia for evaluation of NO_x emission fluxes of INTEX-B, CAPSS, and REAS inventories, Atmos. Chem. Phys., 15(4), 1913–1938, doi:10.5194/acp-15-1913-2015, 2015.

He, L.-Y., Huang, X.-F., Xue, L., Hu, M., Lin, Y., Zheng, J., Zhang, R. and Zhang, Y.-H.: Submicron aerosol analysis and organic source apportionment in an urban atmosphere in Pearl River Delta of China using high-resolution aerosol mass spectrometry, J. Geophys. Res., 116(D12), doi:10.1029/2010JD014566, 2011.

Hodzic, A., Jimenez, J. L., Madronich, S., Canagaratna, M. R., DeCarlo, P. F., Kleinman, L. and Fast, J.: Modeling organic aerosols in a megacity: potential contribution of semi-volatile and intermediate volatility primary organic compounds to secondary organic aerosol formation, Atmos. Chem. Phys., 10(12), 5491–5514, doi:10.5194/acp-10-5491-2010, 2010.

Holben, B. N., Eck, T. F., Slutsker, I., Tanré, D., Buis, J. P., Setzer, A., Vermote, E., Reagan, J. A., Kaufman, Y. J., Nakajima, T., Lavenu, F., Jankowiak, I. and Smirnov, A.: AERONET—A Federated Instrument Network and Data Archive for Aerosol Characterization, Remote Sens. Environ., 66(1), 1–16, doi:10.1016/S0034-4257(98)00031-5, 1998.

Huang, X.-F., He, L.-Y., Hu, M., Canagaratna, M. R., Sun, Y., Zhang, Q., Zhu, T., Xue, L., Zeng, L.-W., Liu, X.-G., Zhang, Y.-H., Jayne, J. T., Ng, N. L. and Worsnop, D. R.: Highly time-resolved chemical characterization of atmospheric submicron particles during 2008 Beijing Olympic Games using an Aerodyne High-Resolution Aerosol Mass Spectrometer, Atmos. Chem. Phys., 10(18), 8933–8945, doi:10.5194/acp-10-8933-2010, 2010.

Karamchandani, P., Santos, L., Sykes, I., Zhang, Y., Tonne, C. and Seigneur, C.: Development and Evaluation of a State-of-the-Science Reactive Plume Model, Environ. Sci. Technol., 34(5), 870–880, doi:10.1021/es990611v, 2000.

Kim, H. S., Song, C. H., Park, R. S., Huey, G. and Ryu, J. Y.: Investigation of ship-plume chemistry using a newly-developed photochemical/dynamic ship-plume model, Atmos. Chem. Phys., 9(19), 7531–7550, doi:10.5194/acp-9-7531-2009, 2009.

Kim, H. S., Kim, Y. H. and Song, C. H.: Ship-plume sulfur chemistry: ITCT 2K2 case study, Sci. Total Environ., 450-451, 178–187, doi:10.1016/j.scitotenv.2013.01.099, 2013.

Kubistin, D., Harder, H., Martinez, M., Rudolf, M., Sander, R., Bozem, H., Eerdekens, G., Fischer, H., Gurk, C., Klüpfel, T., Königstedt, R., Parchatka, U., Schiller, C. L., Stickler, A., Taraborrelli, D., Williams, J. and Lelieveld, J.: Hydroxyl radicals in the tropical troposphere over the Suriname rainforest: comparison of measurements with the box model MECCA, Atmos. Chem. Phys., 10(19), 9705–9728, doi:10.5194/acp-10-9705-2010, 2010.

Lahoz, W. A., Peuch, V.-H., Orphal, J., Attié, J.-L., Chance, K., Liu, X., Edwards, D., Elbern, H., Flaud, J.-M., Claeyman, M. and Amraoui, L. E.: Monitoring Air Quality from Space: The Case for the Geostationary Platform, Bull. Am. Meteorol. Soc., 93(2), 221–233, doi:10.1175/BAMS-D-11-00045.1, 2011.

Lee, J., Kim, J., Song, C. H., Ryu, J.-H., Ahn, Y.-H. and Song, C. K.: Algorithm for retrieval of aerosol optical properties over the ocean from the Geostationary Ocean Color Imager, Remote Sens. Environ., 114(5), 1077–1088, doi:10.1016/j.rse.2009.12.021, 2010.

Lee, J., Kim, J., Yang, P. and Hsu, N. C.: Improvement of aerosol optical depth retrieval from MODIS spectral reflectance over the global ocean using new aerosol models archived from AERONET inversion data and tri-axial ellipsoidal dust database, Atmos. Chem. Phys., 12(15), 7087–7102, doi:10.5194/acp-12-7087-2012, 2012.

Lee, S., Ghim, Y. S., Kim, S.-W. and Yoon, S.-C.: Seasonal characteristics of chemically apportioned aerosol optical properties at Seoul and Gosan, Korea, Atmos. Environ., 43(6), 1320–1328, doi:10.1016/j.atmosenv.2008.11.044, 2009.

Lee, Y. H., Choi, Y. and Ghim, Y. S.: Classification of diurnal patterns of particulate inorganic ions downwind of metropolitan Seoul, in submission, 2015.

Lelieveld, J., Butler, T. M., Crowley, J. N., Dillon, T. J., Fischer, H., Ganzeveld, L., Harder, H., Lawrence, M. G., Martinez, M., Taraborrelli, D. and Williams, J.: Atmospheric oxidation capacity sustained by a tropical forest, Nature, 452(7188), 737–740, doi:10.1038/nature06870, 2008.

Levy, R. C., Remer, L. A., Mattoo, S., Vermote, E. F. and Kaufman, Y. J.: Second-generation operational algorithm: Retrieval of aerosol properties over land from inversion of Moderate Resolution Imaging Spectroradiometer spectral reflectance: NEW MODIS RETRIEVAL OF AEROSOL OVER LAND, J. Geophys. Res. Atmospheres, 112(D13), D13211, doi:10.1029/2006JD007811, 2007.

Liu, Z., Liu, Q., Lin, H.-C., Schwartz, C. S., Lee, Y.-H. and Wang, T.: Three-dimensional variational assimilation of MODIS aerosol optical depth: Implementation and application to a dust storm over East Asia, J. Geophys. Res. Atmospheres, 116(D23), D23206, doi:10.1029/2011JD016159, 2011.

Lu, Z., Streets, D. G., Zhang, Q., Wang, S., Carmichael, G. R., Cheng, Y. F., Wei, C., Chin, M., Diehl, T. and Tan, Q.: Sulfur dioxide emissions in China and sulfur trends in East Asia since 2000, Atmos. Chem. Phys., 10(13), 6311–6331, doi:10.5194/acp-10-6311-2010, 2010.

Malm, W. C. and Hand, J. L.: An examination of the physical and optical properties of aerosols collected in the IMPROVE program, Atmos. Environ., 41(16), 3407–3427, doi:10.1016/j.atmosenv.2006.12.012, 2007.

Martin, R. V., Jacob, D. J., Yantosca, R. M., Chin, M. and Ginoux, P.: Global and regional decreases in tropospheric oxidants from photochemical effects of aerosols, J. Geophys. Res. Atmospheres, 108(D3), 4097, doi:10.1029/2002JD002622, 2003.

Matsui, H., Koike, M., Kondo, Y., Takami, A., Fast, J. D., Kanaya, Y. and Takigawa, M.: Volatility basis-set approach simulation of organic aerosol formation in East Asia: implications for anthropogenic–biogenic interaction and controllable amounts, Atmos. Chem. Phys., 14(18), 9513–9535, doi:10.5194/acp-14-9513-2014, 2014.

Munchak, L. A., Levy, R. C., Mattoo, S., Remer, L. A., Holben, B. N., Schafer, J. S., Hostetler, C. A. and Ferrare, R. A.: MODIS 3 km aerosol product: applications over land in an urban/suburban region, Atmos. Meas. Tech., 6(7), 1747–1759, doi:10.5194/amt-6-1747-2013, 2013.

Myneni, R. B., Hoffman, S., Knyazikhin, Y., Privette, J. L., Glassy, J., Tian, Y., Wang, Y., Song, X., Zhang, Y., Smith, G. R., Lotsch, A., Friedl, M., Morisette, J. T., Votava, P., Nemani, R. R. and Running, S. W.: Global products of vegetation leaf area and fraction absorbed PAR from year one of MODIS data, Remote Sens. Environ., 83(1–2), 214–231, doi:10.1016/S0034-4257(02)00074-3, 2002.

NCL: The NCAR Command Language (Version 6.2.1) [Software], Boulder Colo. UCARNCARCISLVETS, doi:10.5065/D6WD3XH5, 2014.

Otte, T. L. and Pleim, J. E.: The Meteorology-Chemistry Interface Processor (MCIP) for the CMAQ modeling system: updates through MCIPv3.4.1, Geosci. Model Dev., 3(1), 243–256, doi:10.5194/gmd-3-243-2010, 2010.

Park, M. E., Song, C. H., Park, R. S., Lee, J., Kim, J., Lee, S., Woo, J.-H., Carmichael, G. R., Eck, T. F., Holben, B. N., Lee, S.-S., Song, C. K. and Hong, Y. D.: New approach to monitor transboundary particulate pollution over Northeast Asia, Atmos. Chem. Phys., 14(2), 659–674, doi:10.5194/acp-14-659-2014, 2014a.

Park, R. S., Song, C. H., Han, K. M., Park, M. E., Lee, S.-S., Kim, S.-B. and Shimizu, A.: A study on the aerosol optical properties over East Asia using a combination of CMAQ-simulated aerosol optical properties and remote-sensing data via a data assimilation technique, Atmos. Chem. Phys., 11(23), 12275–12296, doi:10.5194/acp-11-12275-2011, 2011.

Park, R. S., Lee, S., Shin, S.-K. and Song, C. H.: Contribution of ammonium nitrate to aerosol optical depth and direct radiative forcing by aerosols over East Asia, Atmos. Chem. Phys., 14(4), 2185–2201, doi:10.5194/acp-14-2185-2014, 2014b.

Pebesma, E.: spacetime: Spatio-Temporal Data in R, J. Stat. Softw., 51(7) [online] Available from: http://www.jstatsoft.org/v51/i07, 2012.

Pebesma, E. J.: Multivariable geostatistics in S: the gstat package, Comput. Geosci., 30(7), 683–691, doi:10.1016/j.cageo.2004.03.012, 2004.

Pope, C. A. and Dockery, D. W.: Health Effects of Fine Particulate Air Pollution: Lines that Connect, J. Air Amp Waste Manag. Assoc., 56(6), 709–742, doi:10.1080/10473289.2006.10464485, 2006.

R Development Core Team: R: A Language and Environment for Statistical Computing, R Foundation for Statistical Computing, Vienna, Austria. [online] Available from: http://www.R-project.org/, 2011.

Reff, A., Bhave, P. V., Simon, H., Pace, T. G., Pouliot, G. A., Mobley, J. D. and Houyoux, M.: Emissions Inventory of $PM_{2.5}$ Trace Elements across the United States, Environ. Sci. Technol., 43(15), 5790–5796, doi:10.1021/es802930x, 2009.

Remer, L. A., Kaufman, Y. J., Tanré, D., Mattoo, S., Chu, D. A., Martins, J. V., Li, R.-R., Ichoku, C., Levy, R. C., Kleidman, R. G., Eck, T. F., Vermote, E. and Holben, B. N.: The MODIS Aerosol Algorithm, Products, and Validation, J. Atmospheric Sci., 62(4), 947–973, doi:10.1175/JAS3385.1, 2005.

Al-Saadi, J., Szykman, J., Pierce, R. B., Kittaka, C., Neil, D., Chu, D. A., Remer, L., Gumley, L., Prins, E., Weinstock, L., MacDonald, C., Wayland, R., Dimmick, F. and Fishman, J.: Improving National Air Quality Forecasts with Satellite Aerosol Observations, Bull. Am. Meteorol. Soc., 86(9), 1249–1261, doi:10.1175/BAMS-86-9-1249, 2005.

Saide, P. E., Carmichael, G. R., Liu, Z., Schwartz, C. S., Lin, H. C., da Silva, A. M. and Hyer, E.: Aerosol optical depth assimilation for a size-resolved sectional model: impacts of observationally constrained, multi-wavelength and fine mode retrievals on regional scale analyses and forecasts, Atmos. Chem. Phys., 13(20), 10425–10444, doi:10.5194/acp-13-10425-2013, 2013.

Sakulyanontvittaya, T., Duhl, T., Wiedinmyer, C., Helmig, D., Matsunaga, S., Potosnak, M., Milford, J. and Guenther, A.: Monoterpene and Sesquiterpene Emission Estimates for the United States, Environ. Sci. Technol., 42(5), 1623–1629, doi:10.1021/es702274e, 2008.

Savage, N. H., Agnew, P., Davis, L. S., Ordóñez, C., Thorpe, R., Johnson, C. E., O'Connor, F. M. and Dalvi, M.: Air quality modelling using the Met Office Unified Model (AQUM OS24-26): model description and initial evaluation, Geosci. Model Dev., 6(2), 353–372, doi:10.5194/gmd-6-353-2013, 2013.

Saxena, P., Belle Hudischewskyj, A., Seigneur, C. and Seinfeld, J. H.: A comparative study of equilibrium approaches to the chemical characterization of secondary aerosols, Atmos. Environ. 1967, 20(7), 1471–1483, doi:10.1016/0004-6981(86)90019-3, 1986.

Schwartz, C. S., Liu, Z., Lin, H.-C. and McKeen, S. A.: Simultaneous three-dimensional variational assimilation of surface fine particulate matter and MODIS aerosol optical depth, J. Geophys. Res. Atmospheres, 117(D13), D13202, doi:10.1029/2011JD017383, 2012.

Seinfeld, J. H. and Pandis, S. N.: Atmospheric chemistry and physics: from air pollution to climate change, John Wiley & Sons., 2012.

Shi, Y., Zhang, J., Reid, J. S., Holben, B., Hyer, E. J. and Curtis, C.: An analysis of the collection 5 MODIS over-ocean aerosol optical depth product for its implication in aerosol assimilation, Atmos. Chem. Phys., 11(2), 557–565, doi:10.5194/acp-11-557-2011, 2011.

Skamarock, W. C. and Klemp, J. B.: A time-split nonhydrostatic atmospheric model for weather research and forecasting applications, J. Comput. Phys., 227(7), 3465–3485, doi:10.1016/j.jcp.2007.01.037, 2008.

Slowik, J. G., Stroud, C., Bottenheim, J. W., Brickell, P. C., Chang, R. Y.-W., Liggio, J., Makar, P. A., Martin, R. V., Moran, M. D., Shantz, N. C., Sjostedt, S. J., van Donkelaar, A., Vlasenko, A., Wiebe, H. A., Xia, A. G., Zhang, J., Leaitch, W. R. and Abbatt, J. P. D.: Characterization of a large biogenic secondary organic aerosol event from eastern Canadian forests, Atmos. Chem. Phys., 10(6), 2825–2845, doi:10.5194/acp-10-2825-2010, 2010.

Smith, S. J., van Aardenne, J., Klimont, Z., Andres, R. J., Volke, A. and Delgado Arias, S.: Anthropogenic sulfur dioxide emissions: 1850–2005, Atmos. Chem. Phys., 11(3), 1101–1116, doi:10.5194/acp-11-1101-2011, 2011.

Song, C. H. and Carmichael, G. R.: The aging process of naturally emitted aerosol (sea-salt and mineral aerosol) during long range transport, Atmos. Environ., 33(14), 2203–2218, doi:10.1016/S1352-2310(98)00301-X, 1999.

Song, C. H. and Carmichael, G. R.: Gas-Particle Partitioning of Nitric Acid Modulated by Alkaline Aerosol, J. Atmospheric Chem., 40(1), 1–22, 2001.

Song, C. H., Chen, G., Hanna, S. R., Crawford, J. and Davis, D. D.: Dispersion and chemical evolution of ship plumes in the marine boundary layer: Investigation of O3/NOy/HOx chemistry, J. Geophys. Res. Atmospheres, 108(D4), 4143, doi:10.1029/2002JD002216, 2003.

Song, C. H., Park, M. E., Lee, K. H., Ahn, H. J., Lee, Y., Kim, J. Y., Han, K. M., Kim, J., Ghim, Y. S. and Kim, Y. J.: An investigation into seasonal and regional aerosol characteristics in East Asia using model-predicted and remotely-sensed aerosol properties, Atmos. Chem. Phys., 8(22), 6627–6654, doi:10.5194/acp-8-6627-2008, 2008.

Song, C. H., Kim, H. S., von Glasow, R., Brimblecombe, P., Kim, J., Park, R. J., Woo, J. H. and Kim, Y. H.: Source identification and budget analysis on elevated levels of formaldehyde within the ship plumes: a ship-plume photochemical/dynamic model analysis, Atmos. Chem. Phys., 10(23), 11969–11985, doi:10.5194/acp-10-11969-2010, 2010.

Sörgel, M., Regelin, E., Bozem, H., Diesch, J.-M., Drewnick, F., Fischer, H., Harder, H., Held, A., Hosaynali-Beygi, Z., Martinez, M. and Zetzsch, C.: Quantification of the unknown HONO daytime source and its relation to NO_2, Atmos. Chem. Phys., 11(20), 10433–10447, doi:10.5194/acp-11-10433-2011, 2011.

Stelson, A. W., Bassett, M. E. and Seinfeld, J. H.: Thermodynamic equilibrium properties of aqueous solutions of nitrate, sulfate and ammonium., ACID PRECIP SER 1984, 1984.

Stemmler, K., Ammann, M., Donders, C., Kleffmann, J. and George, C.: Photosensitized reduction of nitrogen dioxide on humic acid as a source of nitrous acid, Nature, 440(7081), 195–198, doi:10.1038/nature04603, 2006.

Tang, Y., Chai, T., Pan, L., Lee, P., Tong, D., Kim, H.-C. and Chen, W.: Using optimal interpolation to assimilate surface measurements and satellite AOD for ozone and $PM_{2.5}$: A case study for July 2011, Journal of the Air & Waste Management Association, 65(10), 1206–1216, doi:10.1080/10962247.2015.1062439, 2015.

Tsimpidi, A. P., Karydis, V. A., Zavala, M., Lei, W., Molina, L., Ulbrich, I. M., Jimenez, J. L. and Pandis, S. N.: Evaluation of the volatility basis-set approach for the simulation of organic aerosol formation in the Mexico City metropolitan area, Atmos. Chem. Phys., 10(2), 525–546, doi:10.5194/acp-10-525-2010, 2010.

Wiedinmyer, C., Akagi, S. K., Yokelson, R. J., Emmons, L. K., Al-Saadi, J. A., Orlando, J. J. and Soja, A. J.: The Fire INventory from NCAR (FINN): a high resolution global model to estimate the emissions from open burning, Geosci. Model Dev., 4(3), 625–641, doi:10.5194/gmd-4-625-2011, 2011.

Willmott, C. and Matsuura, K.: Advantages of the mean absolute error (MAE) over the root mean square error (RMSE) in assessing average model performance, Clim. Res., 30, 79–82, doi:10.3354/cr030079, 2005.

Willmott, C. J.: On the Validation of Models, Phys. Geogr., 2(2), 184–194, doi:10.1080/02723646.1981.10642213, 1981.

Willmott, C. J., Matsuura, K. and Robeson, S. M.: Ambiguities inherent in sums-of-squares-based error statistics, Atmos. Environ., 43(3), 749–752, doi:10.1016/j.atmosenv.2008.10.005, 2009.

Woo, J.-H., Choi, K.-C., Kim, H. K., Baek, B. H., Jang, M., Eum, J.-H., Song, C. H., Ma, Y.-I., Sunwoo, Y., Chang, L.-S. and Yoo, S. H.: Development of an anthropogenic emissions processing system for Asia using SMOKE, Atmos. Environ., 58, 5–13, doi:10.1016/j.atmosenv.2011.10.042, 2012.

Wyat Appel, K., Bhave, P. V., Gilliland, A. B., Sarwar, G. and Roselle, S. J.: Evaluation of the community multiscale air quality (CMAQ) model version 4.5: Sensitivities impacting model performance; Part II—particulate matter, Atmos. Environ., 42(24), 6057–6066, doi:10.1016/j.atmosenv.2008.03.036, 2008.

Zhang, Q., Jimenez, J. L., Canagaratna, M. R., Allan, J. D., Coe, H., Ulbrich, I., Alfarra, M. R., Takami, A., Middlebrook, A. M., Sun, Y. L., Dzepina, K., Dunlea, E., Docherty, K., DeCarlo, P. F., Salcedo, D., Onasch, T., Jayne, J. T., Miyoshi, T., Shimono, A., Hatakeyama, S., Takegawa, N., Kondo, Y., Schneider, J., Drewnick, F., Borrmann, S., Weimer, S., Demerjian, K., Williams, P., Bower, K., Bahreini, R., Cottrell, L., Griffin, R. J., Rautiainen, J., Sun, J. Y., Zhang, Y. M. and Worsnop, D. R.: Ubiquity and dominance of oxygenated species in organic aerosols in anthropogenically-influenced Northern Hemisphere midlatitudes, Geophys. Res. Lett., 34(13), L13801, doi:10.1029/2007GL029979, 2007.

Zhang, X. Y., Wang, Y. Q., Niu, T., Zhang, X. C., Gong, S. L., Zhang, Y. M. and Sun, J. Y.: Atmospheric aerosol compositions in China: spatial/temporal variability, chemical signature, regional haze distribution and comparisons with global aerosols, Atmos. Chem. Phys., 12(2), 779–799, doi:10.5194/acp-12-779-2012, 2012.

Zhou, X., Zhang, N., TerAvest, M., Tang, D., Hou, J., Bertman, S., Alaghmand, M., Shepson, P. B., Carroll, M. A., Griffith, S., Dusanter, S. and Stevens, P. S.: Nitric acid photolysis on forest canopy surface as a source for tropospheric nitrous acid, Nat. Geosci., 4(7), 440–443, doi:10.1038/ngeo1164, 2011.

Zoogman, P., Jacob, D. J., Chance, K., Liu, X., Lin, M., Fiore, A. and Travis, K.: Monitoring high-ozone events in the US Intermountain West using TEMPO geostationary satellite observations, Atmos. Chem. Phys., 14(12), 6261–6271, doi:10.5194/acp-14-6261-2014, 2014.

Table 1. WRF and CMAQ model configurations.

	WRF (ver. 3.5.1)		CMAQ (ver. 5.0.1)
Microphysics scheme	WRF single-moment 3 class	Chemical mechanism	SAPRC-99
Long- and short-wave radiation	Rapid Radiation Transfer Model for GCMs (RRTMG)	Aerosol module	AERO-6
Planetary boundary layer	Yonsei University scheme	Chemistry solver	Euler backward iterative (EBI) solver
Land-surface model	Noah-MP	Photolysis module	In-line photolysis calculations

Table 2. Values used in observation operators for estimating aerosol optical properties (AOPs).

Method for estimating aerosol optical properties	Aerosol speciation	Hygroscopic aerosols	α_{OC}[1]	α_{BC}[2]	α_{SSAM}[3]	α_{SSCM}[4]
Chin et al. (2002)	$(NH_4)_2SO_4$, OC, BC, dust (7 size bins), sea-salt (2 modes)	$(NH_4)_2SO_4$, OC, BC, sea-salt	2.67	9.28	1.15	0.13
Martin et al. (2003)	$(NH_4)_2SO_4$, OC, BC, dust (7 size bins), sea-salt (2 modes)	$(NH_4)_2SO_4$, OC, BC, sea-salt	2.82	8.05	2.37	0.94
Malm and Hand (2007)	NH_4NO_3, $(NH_4)_2SO_4$, organic matter, soil, coarse mass, sea-salt	NH_4NO_3, $(NH_4)_2SO_4$, sea-salt	4.00	10.00	1.37	1.37

Dry mass extinction efficiencies (m^2 g^{-1}) at 550nm of [1] OC, [2] BC, [3] sea-salt in accumulation mode and [4] sea-salt in coarse mode

Note: In cases of Chin et al. (2002) and Martin et al. (2003), the AOPs for sulfate were used for calculating AOPs for NH_4NO_3 and $(NH_4)_2SO_4$.

Table 3. Definition of model configurations.

Configuration	Observation operator	Control variable
A1	Chin et al. (2002)	Total aerosol mass concentration
A2		SO_4^{2-} mass concentration
A3		SO_4^{2-} and OAs mass concentration
A4		SO_4^{2-}, NO_3^-, NH_4^+ and OAs mass concentration
B1	Martin et al. (2003)	Total aerosol mass concentration
B2		SO_4^{2-} mass concentration
B3		SO_4^{2-} and OAs mass concentration
B4		SO_4^{2-}, NO_3^-, NH_4^+ and OAs mass concentration
C1	Malm and Hand (2007)	Total aerosol mass concentration
C2		SO_4^{2-} mass concentration
C3		SO_4^{2-} and OAs mass concentration
C4		SO_4^{2-}, NO_3^-, NH_4^+ and OAs mass concentration

Table 4. Performance metrics for AOD and PM_{10} hindcasts on the ten selected episodes at six AERONET sites and nearby NAMIS PM_{10} stations in SMA.

Configuration	AOD (N[1] = 277)								PM_{10} (N =340)							
	IOA[2]	MFE[3]	MFB[4]	R[5]	RMSE[6]	MB[7]	MNE[8]	MNB[9]	IOA	MFE	MFB	R	RMSE[10]	MB[10]	MNE	MNB
noSTK	0.48	113.2	-113.2	0.61	0.60	-0.53	70.0	-70.0	0.47	89.0	-88.5	0.54	55.15	-48.40	58.9	-58.4
A1	0.62	37.4	-22.1	0.46	0.36	-0.16	32.5	-13.7	0.60	35.4	-22.7	0.44	36.07	-15.80	31.1	-14.7
A2	0.60	39.8	-20.9	0.41	0.37	-0.15	35.8	-11.3	0.58	39.4	-34.7	0.50	37.13	-24.65	31.6	-25.8
A3	0.63	38.7	-22.5	0.46	0.36	-0.16	34.0	-13.5	0.64	33.0	-23.1	0.52	33.15	-17.07	28.4	-16.2
A4	0.63	37.4	-22.0	0.47	0.35	-0.16	32.6	-13.5	0.64	36.2	-28.3	0.53	34.58	-19.79	30.3	-20.4
B1	0.54	43.1	-27.1	0.33	0.40	-0.18	36.4	-16.2	0.53	41.1	-30.0	0.31	40.01	-20.90	33.9	-20.0
B2	0.51	44.7	-25.2	0.27	0.41	-0.17	39.5	-13.3	0.53	43.8	-39.2	0.37	40.94	-27.50	34.1	-28.5
B3	0.56	42.3	-25.8	0.35	0.39	-0.18	36.6	-15.2	0.56	38.0	-29.6	0.39	37.43	-21.65	31.2	-21.0
B4	0.55	41.9	-24.7	0.34	0.39	-0.17	36.3	-14.2	0.56	40.7	-33.9	0.42	38.30	-23.84	32.8	-24.4
C1	0.50	44.4	-37.5	0.28	0.43	-0.26	34.3	-26.3	0.55	35.8	-14.5	0.32	38.41	-9.82	33.4	-5.4
C2	0.47	45.7	-34.2	0.20	0.43	-0.24	36.7	-22.7	0.55	36.3	-26.0	0.37	36.86	-19.43	30.3	-17.6
C3	0.53	41.7	-30.5	0.34	0.40	-0.22	34.1	-20.5	0.60	32.9	-19.6	0.44	34.07	-14.92	29.1	-12.5
C4	0.53	41.7	-32.4	0.35	0.41	-0.23	32.4	-22.6	0.61	34.8	-21.8	0.44	34.78	-15.68	30.4	-14.0

[1] the number of paired data, [2] index of agreement, [3] mean fractional error, [4] mean fractional bias, [5] Pearson product-moment correlation coefficient, [6] root mean square error, [7] mean bias, [8] mean normalized error, and [9] mean normalized bias. The units of all of metrics are dimensionless except [10] for $\mu g\ m^{-3}$.

Table 5. Performance metrics for PM_{10} hindcasting on the ten selected episodes at 58 NAMIS PM_{10} stations in SMA. Abbreviations are the same as those in Table 3.

Configuration	H+1 to H+6 (N = 4823)								H+7 to H+12 (N = 4921)							
	IOA	MFE	MFB	R	RMSE	MB	MNE	MNB	IOA	MFE	MFB	R	RMSE	MB	MNE	MNB
noSTK	0.45	99.6	-98.7	0.44	62.98	-54.59	63.9	-62.6	0.55	64.7	-36.9	0.30	56.76	-17.77	56.5	-12.9
A1	0.62	42.2	-30.9	0.47	40.64	-21.41	35.6	-19.7	0.62	43.9	1.5	0.37	49.17	5.27	51.2	19.1
A2	0.57	49.1	-43.4	0.48	43.81	-30.49	38.5	-30.4	0.60	45.1	-4.0	0.34	49.81	0.60	49.9	13.1
A3	0.64	40.5	-30.4	0.50	39.46	-21.83	34.2	-20.1	0.63	43.5	5.8	0.39	50.51	9.17	52.7	23.9
A4	0.63	44.6	-36.3	0.52	40.70	-24.99	36.3	-24.7	0.62	43.6	1.2	0.38	49.44	5.10	50.6	18.5
B1	0.54	48.8	-39.6	0.35	45.12	-27.64	38.8	-26.1	0.58	46.0	-3.6	0.31	49.18	0.71	50.8	14.1
B2	0.51	53.9	-48.9	0.36	47.76	-34.14	41.0	-33.9	0.59	46.3	-7.4	0.33	48.73	-2.37	49.1	9.3
B3	0.56	45.9	-37.9	0.40	43.36	-27.48	36.9	-25.8	0.61	44.6	0.7	0.35	48.81	4.07	51.0	17.9
A4	0.56	49.7	-43.0	0.43	44.46	-30.05	38.9	-29.6	0.60	45.2	-3.1	0.34	48.87	1.07	50.0	14.0
C1	0.60	40.4	-22.7	0.39	40.82	-15.98	35.9	-11.7	0.58	45.9	6.6	0.32	51.68	9.84	56.0	26.5
C2	0.56	43.7	-34.3	0.40	42.22	-25.43	35.6	-22.9	0.58	45.9	2.0	0.31	51.37	5.63	53.6	20.7
C3	0.63	39.0	-27.3	0.47	39.00	-20.13	33.3	-17.5	0.61	44.1	7.3	0.37	51.46	10.64	54.3	26.3
C4	0.63	41.2	-29.9	0.48	39.45	-21.30	34.5	-19.4	0.61	44.2	4.7	0.36	50.69	8.29	53.2	23.2

Table S1. Performance metrics for AOD and PM_{10} hindcasts from 7 March 12:00 to 19 March 11:00 at six AERONET sites and nearby NAMIS PM_{10} stations in SMA.

Configuration	AOD (N = 219)								PM_{10} (N =1664)							
	IOA	MFE	MFB	R	RMSE	MB	MNE	MNB	IOA	MFE	MFB	R	RMSE	MB	MNE	MNB
noSTK	0.68	99.21	-98.09	0.69	0.37	-0.29	63.77	-62.49	0.54	63.74	-37.91	0.28	31.26	-12.67	56.78	-13.71
H+0 to H+23	0.73	60.65	-57.90	0.74	0.30	-0.22	43.95	-40.68	0.59	50.49	3.45	0.36	31.68	5.36	69.27	34.03
H+24 to H+47	0.69	81.76	-76.44	0.68	0.34	-0.25	55.16	-48.89	0.57	53.28	-14.36	0.31	30.32	-3.50	58.50	9.36

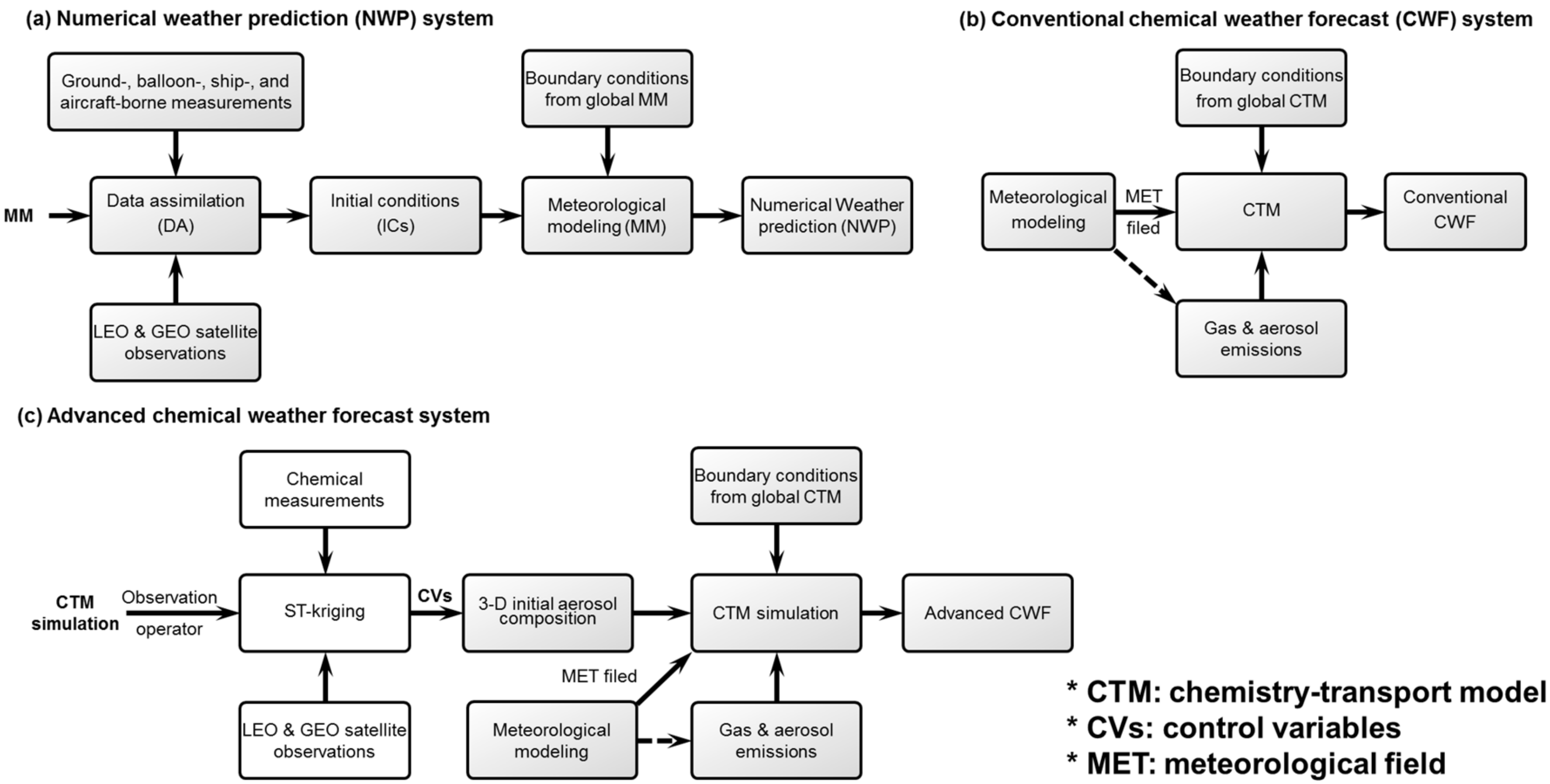

Figure 1. General structure of a) numerical weather prediction (NWP), b) conventional chemical whether forecast CWF), and c) advanced chemical weather forecast system.

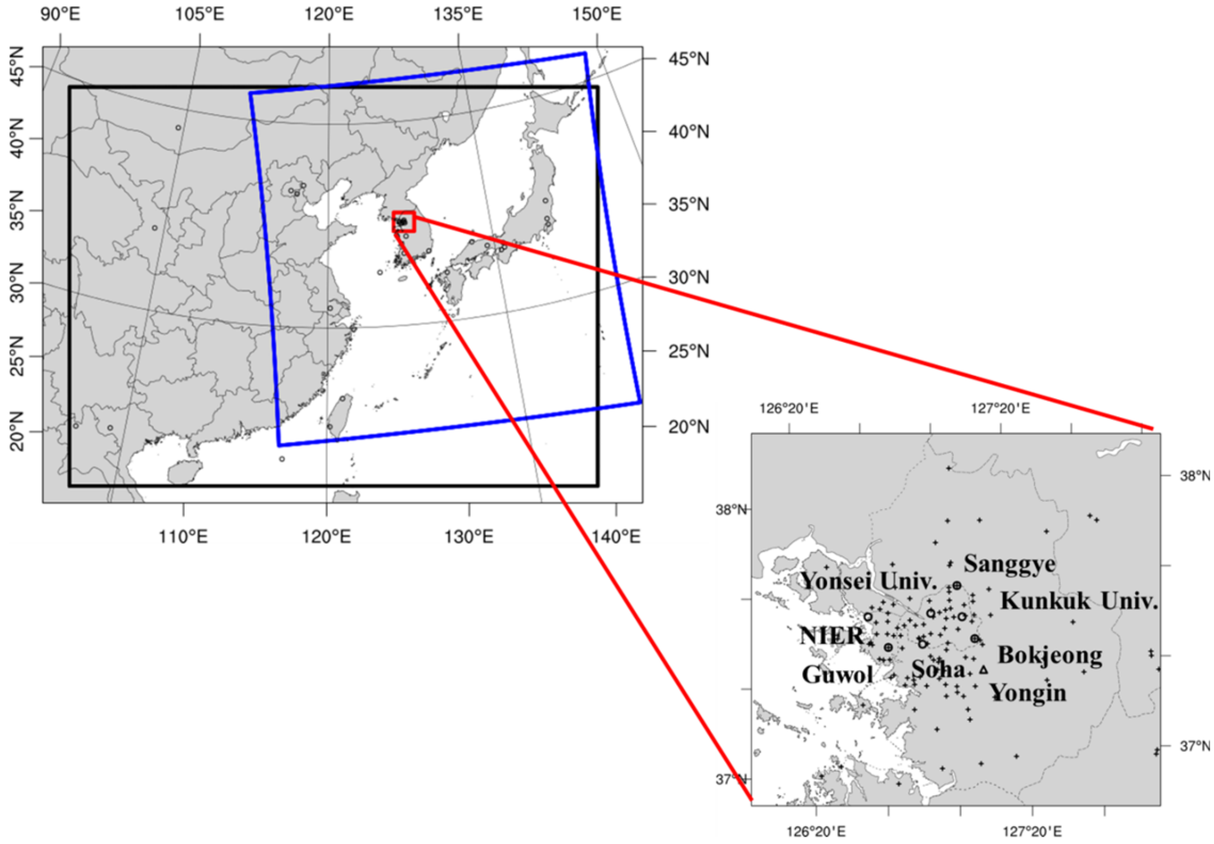

Figure 2. Domains of CMAQ model simulations (black), GOCI sensor coverage (blue), and Seoul Metropolitan area (red). Also shown are seven AERONET level-2 sites (circles), 58 NAMIS PM_{10} sites (crosses), and a PM composition observation site (triangle) in greater Seoul area, respectively.

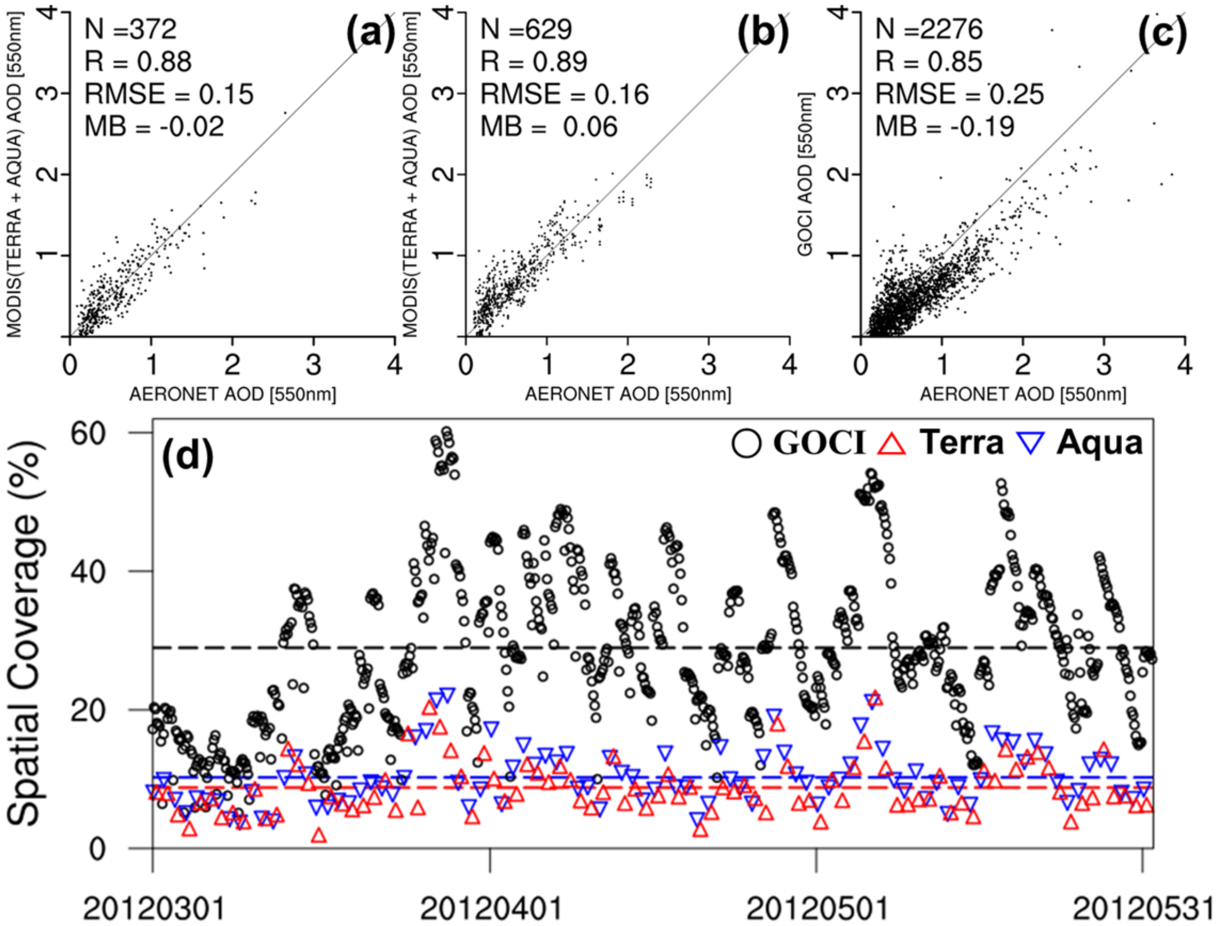

Figure 3. Scatter plots of (a) 10 km Aqua/Terra MODIS AODs vs. AERONET level-2 AODs , (b) 3 km Aqua/Terra MODIS AODs vs. AERONET level-2 AODs and (c) GOCI AODs vs. AERONET level-2 AODs at 550 nm during the DRAGON campaign over the GOCI domain. N, R, RMSE, and MB represent the number of observations, the regression coefficient, root mean square error, and mean bias, respectively. Hourly-resolved Aqua/Terra MODIS and GOCI spatial coverages (%) are also shown in the panel (d) from 1 March to 31 May, 2012.

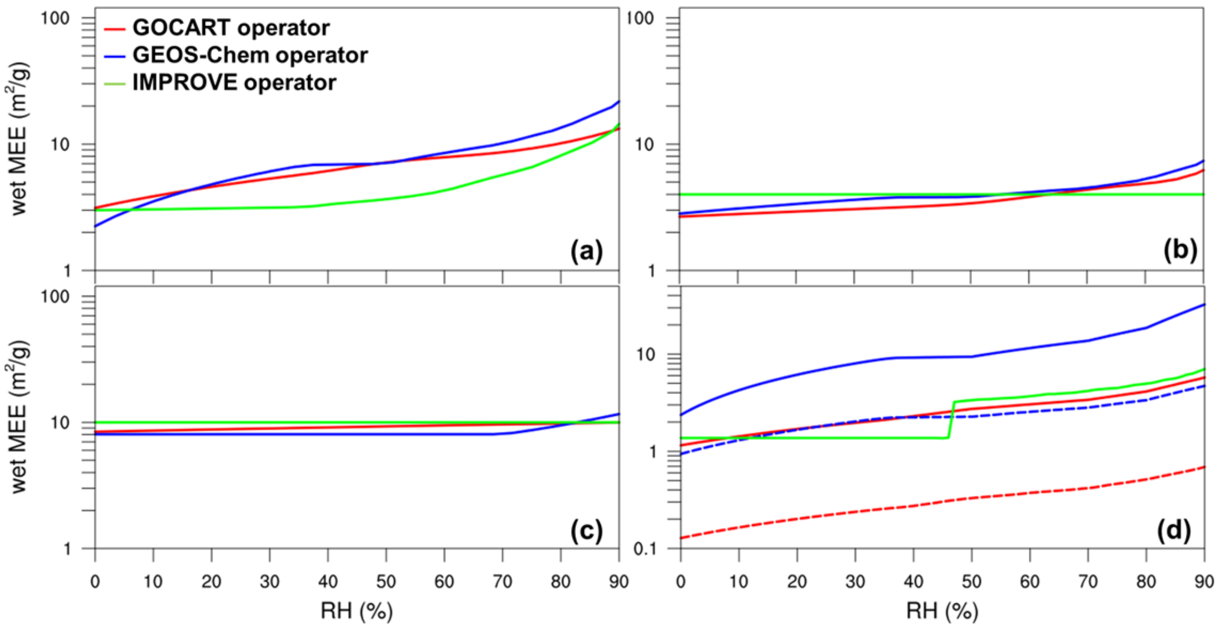

Figure 4. Mass extinction efficiencies (MEEs) calculated for (a) SO_4^{2-}, NO_3^-, and NH_4^+, (b) OAs, (c) BC and (d) sea-salt at a wavelength of 550 nm as a function of RH at a wavelength of 550 nm as a function of relative humidity (%) from three observation operators. In cases of GOCART operator and GEOS-Chem operator, 50% of OAs and 20% of BC are assumed to be hydrophilic. In sea-salt MEEs, accumulate mode and coarse mode are represented as solid lines and dash lines, respectively.

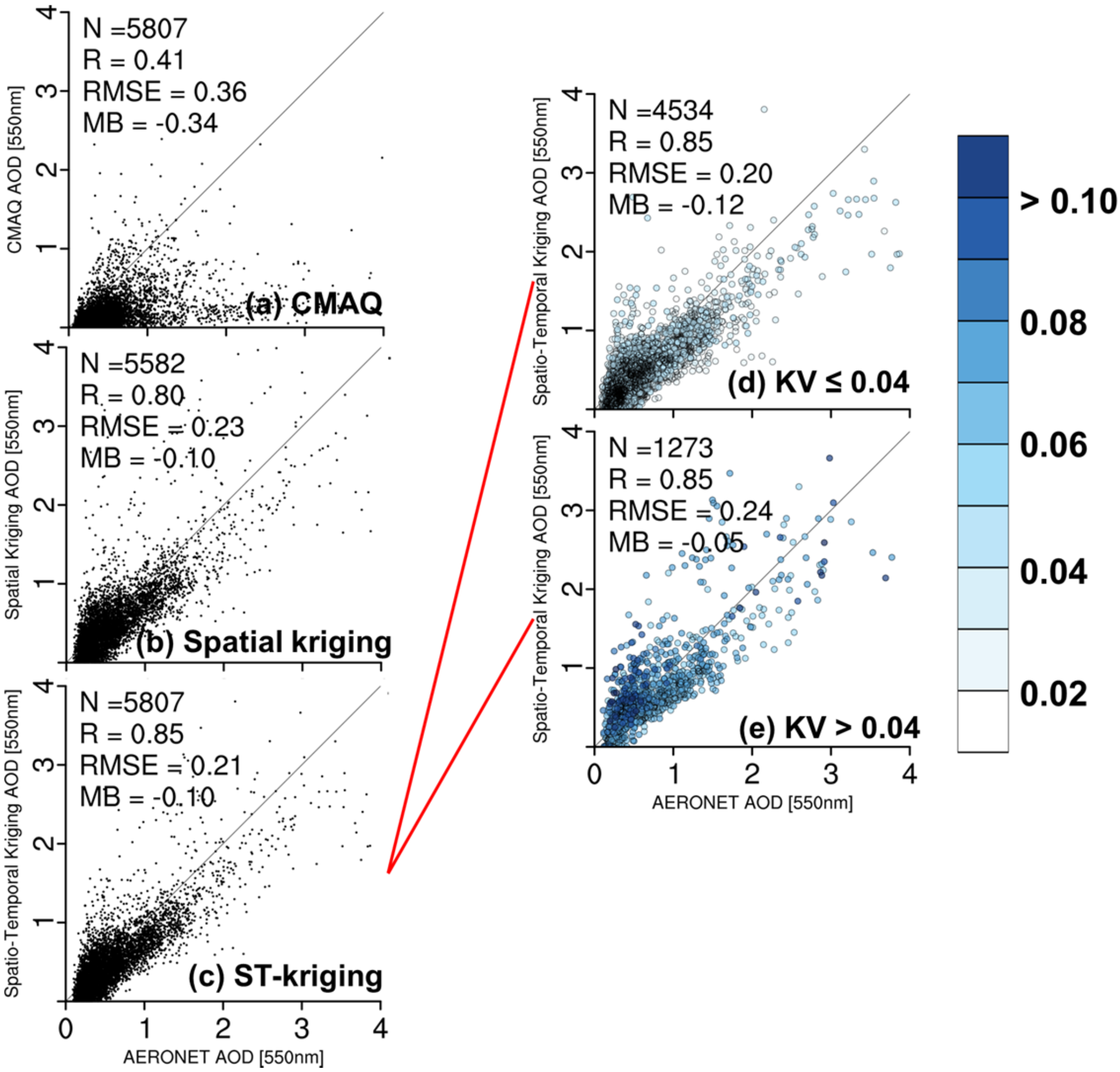

Figure 5. Scatter plots of (a) background CMAQ model AODs, (b) spatial kriging AODs, and c) ST-kriging AODs vs. AERONET level-2 AODs at 550 nm. Plots of ST-kriging with kriging variances (KVs) less equal 0.04 (d) and larger than 0.04 (e) are also shown. The color scale shown in Fig. 5 (e) presents the KVs of ST-kriging AODs. The number of AOD in (b) is smaller than those of (a) and (c) due to the missing hourly AOD fields by the anomaly in GOCI.

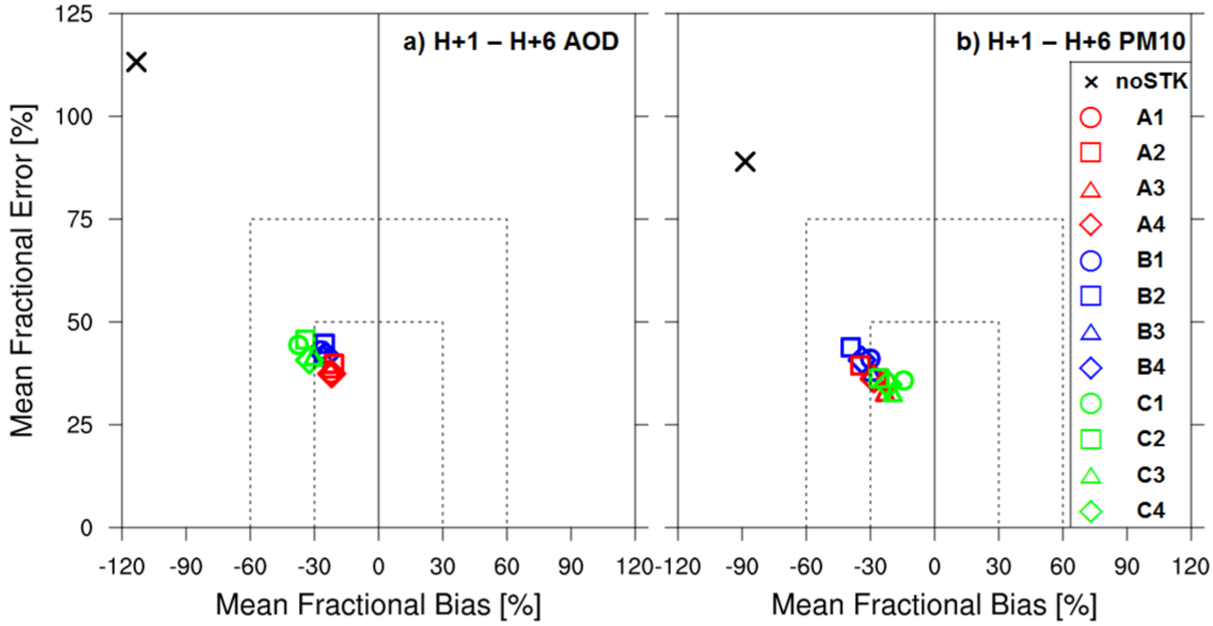

Figure 6. Soccer plot analysis for AOD (left panel) and PM_{10} (right panel) data from the first 6-h observations and the modeld data at six selected sites. BL (denoted by black diamond) represents the case of bilinear interpolation method discussed in Sect. 3. 2.

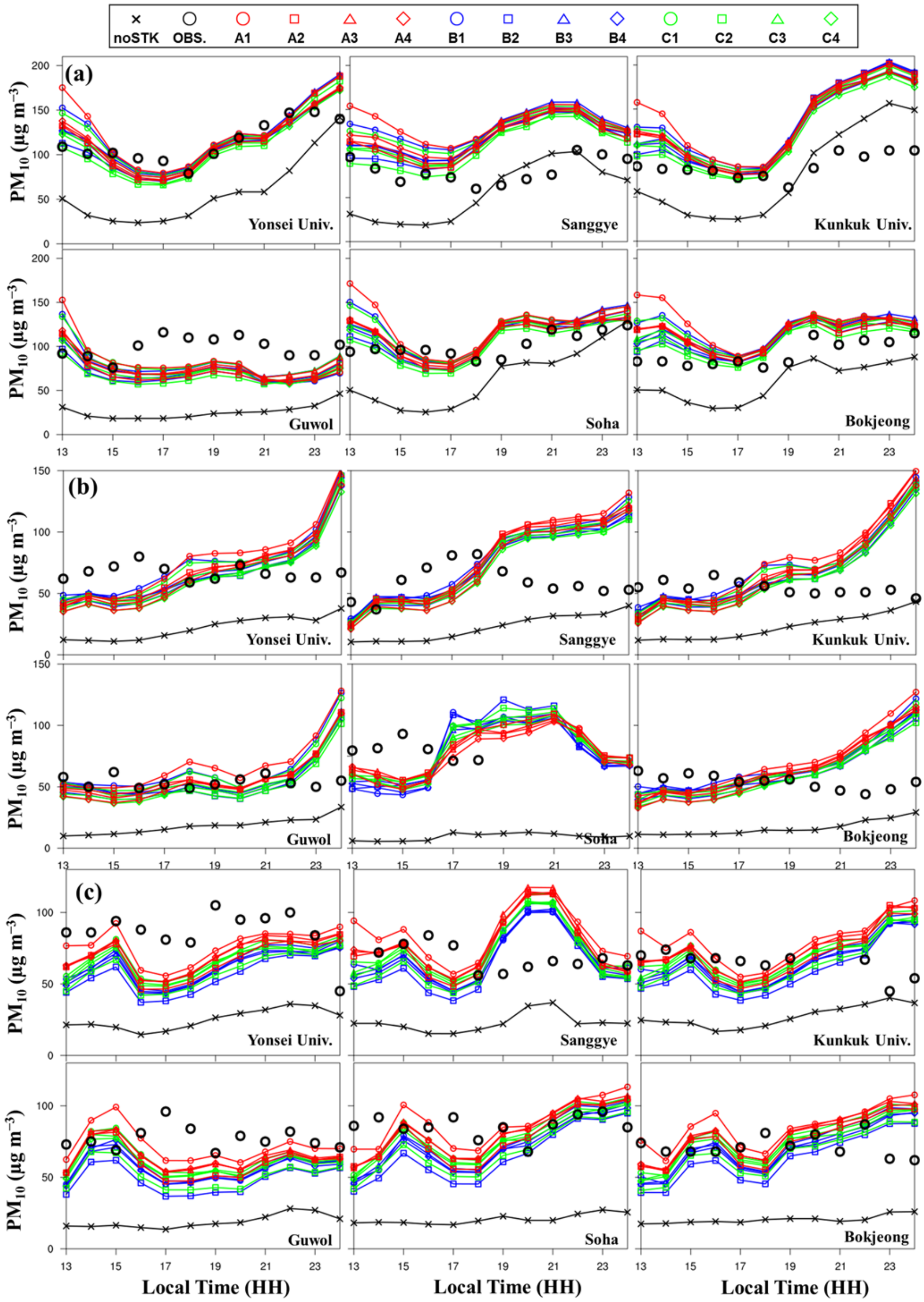

Figure 7. Time series of hourly PM_{10} for the six sites over SMA for 9 April (a), for 6 May (b), and for 16 May (c) in 2012. Observed concentrations are shown as the black circle and the model outputs as the colored line with their own markers explained in the legend.

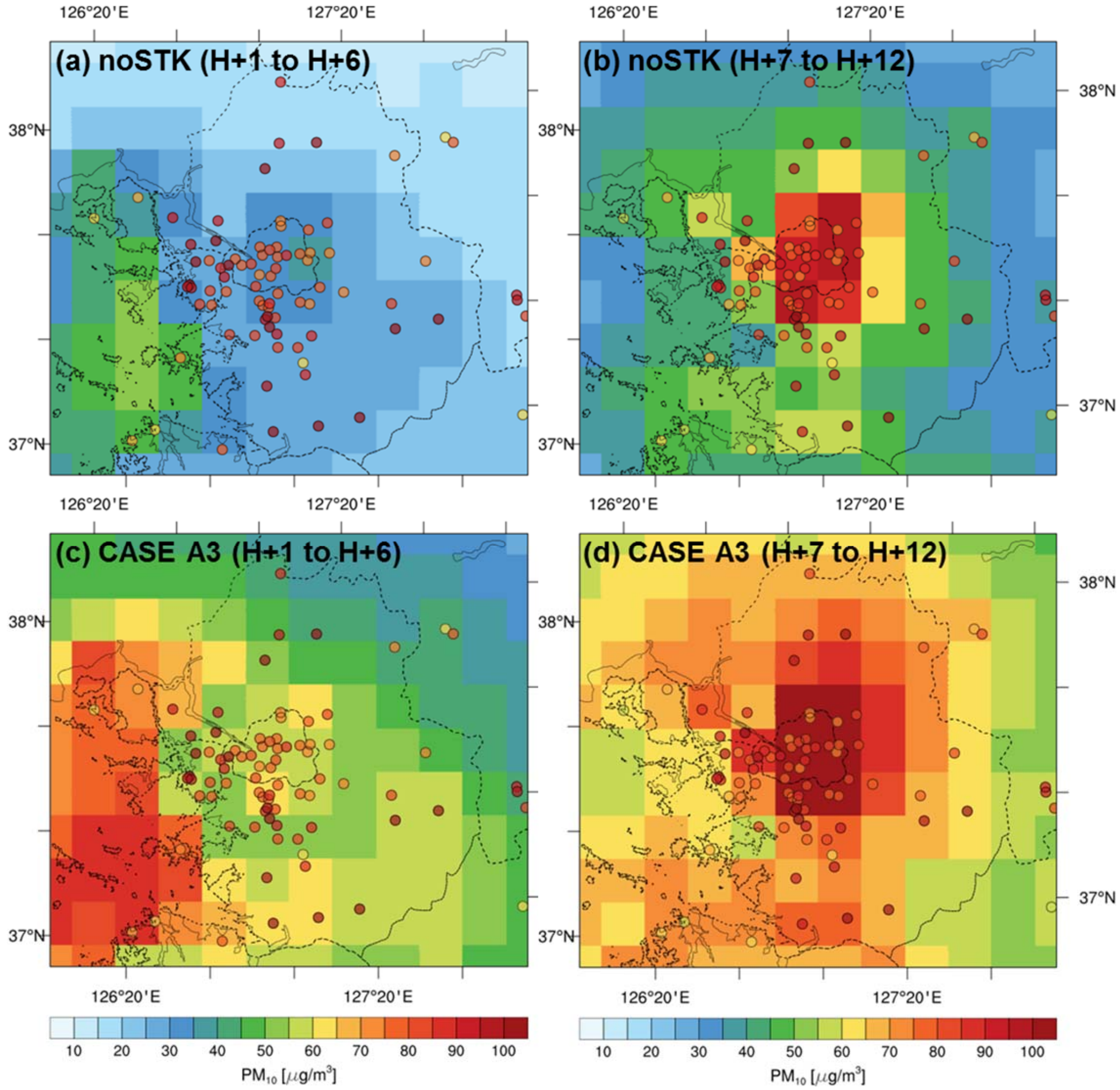

Figure 8. Averaged PM_{10} of noSTK case from H+1 to H+6 (a) and from H+7 to H+13 (b), and the averaged concentrations of case A3 at the same time series ((c) and (d)) for the selected ten days. Averaged NAMIS PM_{10} observations are shown with colored circles.

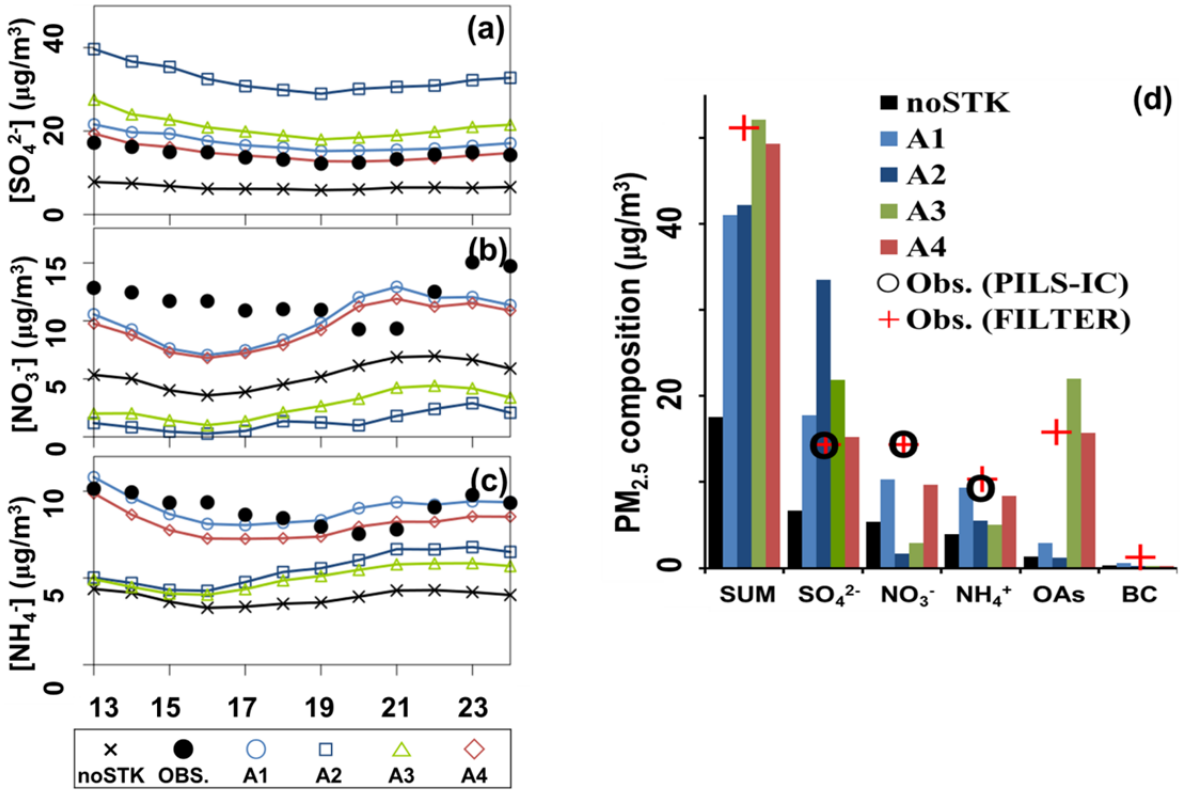

Figure 9. Time-series comparison of 1-hr averaged (a) SO_4^{2-}, (b) NO_3^-, and (c) NH_4^+ concentrations measured from PILS-IC instrument and model-predicted concentrations. In panel (d), 24-h averaged aerosol concentration in $PM_{2.5}$ from observations (PILS-IC instrument and low air volume sampler with Teflon filter) are compared with hindcast concentrations at the Yongin City site for ten selected episodes.

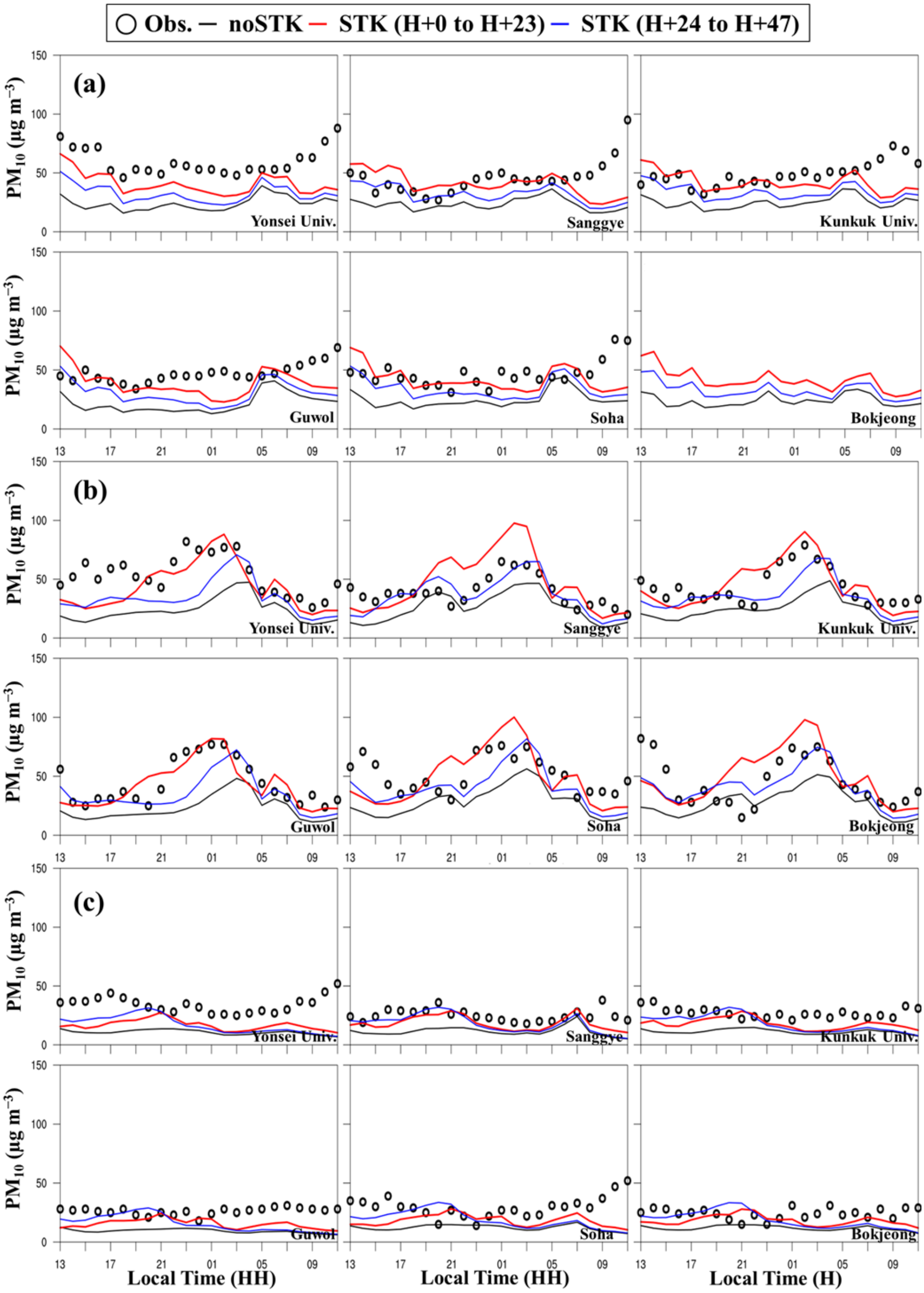

Figure 10. Time series of hourly PM_{10} at six sites in SMA for 8 March (a), for 10 March (b), and for 11 March (c) in 2012. Observed concentrations are denoted as black circles and the modelled concentrations are as colored lines.

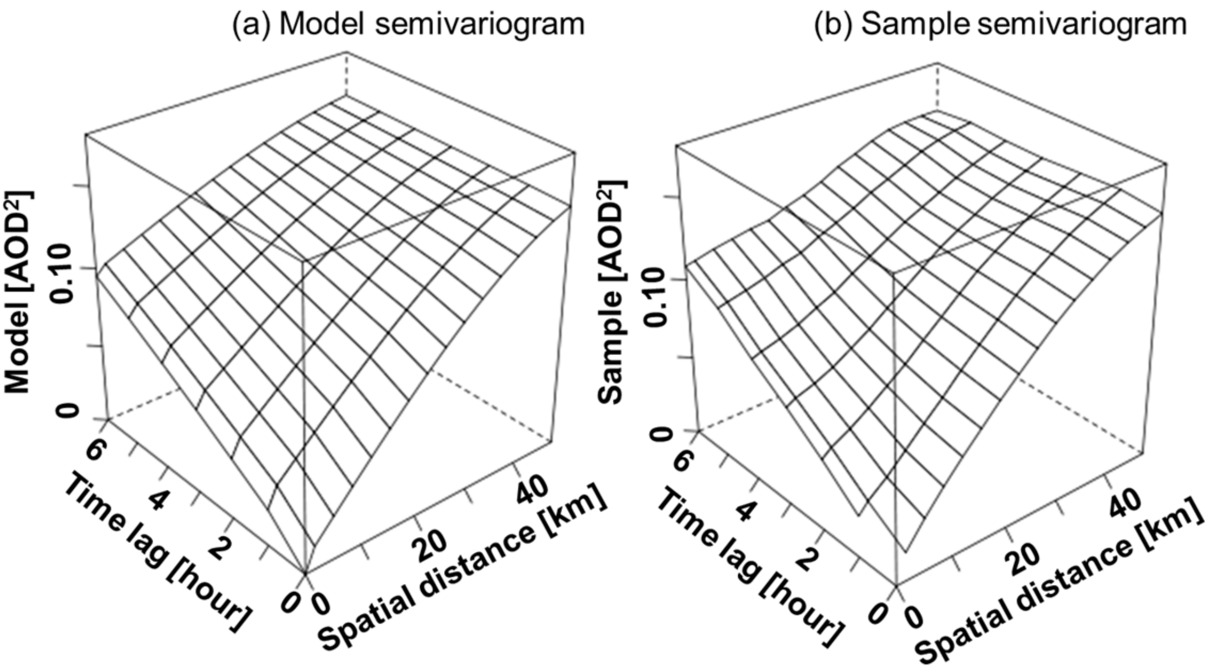

Figure A1. Daily three-dimensional semivariogram from fitted by the spherical model (a), and a sample semivariogram from the GOCI AOD data (b) on 8 April, 2012.

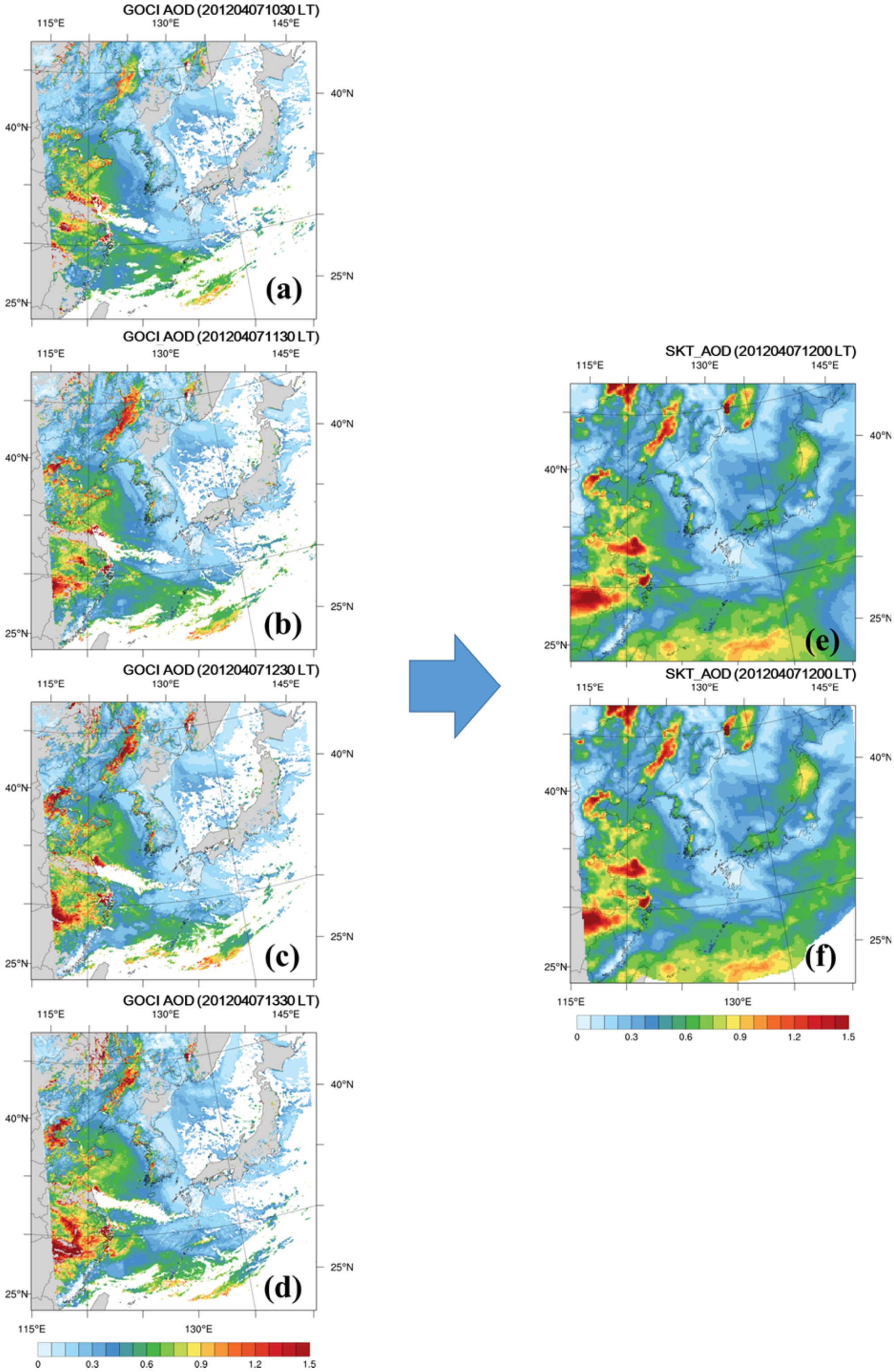

Figure A2. Spatial distributions of GOCI AOD from 10:30 to 13:30 LT ((a) to (d)) and ST-kriging AOD at 12:00 LT (e) on 7 April, 2012. The ST-kriging AOD at 12:00 LT with a criteria of kriging variances (KVs) less than 0.04 is also shown in (f).